

Iopamidol as MRI-CEST contrast agent for improved infection detection on mesoporous TiO₂-functionalised biomedical implants

Master's thesis in Materials Engineering

Supervisors:

Martin Andersson
Mats Hulander
Giancarlo Cicero

Candidate:

Walter Alabiso

MASTER'S THESIS 2019

**A novel technique for investigating
on infections via imaging**

Master's thesis in Materials Engineering

WALTER ALABISO



CHALMERS
UNIVERSITY OF TECHNOLOGY

Department of Chemistry and Chemical Engineering
CHALMERS UNIVERSITY OF TECHNOLOGY
Gothenburg, Sweden 2019

"Iopamidol as MRI-CEST contrast agent for improved infection detection on mesoporous TiO₂-functionalised biomedical implants."

© WALTER ALABISO, mat. 253001, 2019.

Supervisors:

Martin Andersson, Professor at Chalmers Tekniska Högskola, Göteborg, Sweden. Chemistry and Chemical Engineering, Applied Surface Chemistry.

Giancarlo Cicero, Associate Professor (L.240) at DISAT – Department of Applied Science and Technology, Politecnico di Torino, Turin, Italy. Chemical and Materials Engineering.

Master's Thesis 2019
Department of Chemistry and Chemical Engineering
Chalmers University of Technology
SE-412 96 Gothenburg
Telephone +46 31 772 1000

Cover: TEM image showing a mesoporous randomly-ordered structure observable at moderate magnification.

Typeset in L^AT_EX
Printed by Chalmers Reproservice
Gothenburg, Sweden 2019

Acknowledgements

I had a great opportunity to immerse in a vast and active research environment here at Chalmers Tekniska Högskola. I took part of a forward-looking and captivating project, with a lot of precious contributors who helped me achieve this work. Therefore, I would like to explicitly thank **Shitanshu Devrani** for helping me out with the lab work. He has been a serious hard-worker as well as a good friend throughout the duration of this project. A key-role was also played by **Mats Hulander**, who instructed me and Shitanshu about the rules to be observed in the laboratory, and trained us to use the relevant apparatuses properly and safely. Thanks to **Anne Wendel** for guiding us through BET and XPS and **Antiope Lotsari** for helping with TEM. We also received a precious contribution from **Patrick Jarvoll**, Karolinska Institutet, Stockholm for MRI testing, which we are grateful for. Finally, of course, special thanks to my supervisor **Martin Andersson** who granted me this opportunity and helped me cultivate my interest and skills in the biomaterials field.

Walter Alabiso, Gothenburg, May 2019

Abstract

This work presents a novel approach for detecting infections on prosthetic implants via imaging, which is currently a crucial problem in the biomedical sector. For this purpose, a mesoporous titania layer (pore size ~ 6 nm) was produced via self-assembly of Titanium (IV) Butoxide and Pluronic P123 as templating agent. Its role is to coat a prosthetic device so as to guarantee a functionalised active surface, able to integrate correctly with human tissues as well as, most importantly, to carry a specific contrast agent for MRI in its pores. Iopamidol was selected as a drug for MRI-CEST, which would give birth to a signal that is promptly related to local pH changes in the tissues surrounding the prosthesis. This procedure would eventually result in pH-mapping the affected zone, thus helping the surgeon follow the clinical situation in a non-invasive manner. The produced layer was extensively characterised. SEM and TEM allowed concluding that our coating has a 200 nm thick disordered mesoporous structure. From BET, average pore size is 5.7 nm, and the estimated lower bounds for specific volume and specific surface area are $V_s = 0.031 \text{ cm}^3 \text{ g}^{-1}$, and $SA_{BET} = 21.32 \text{ m}^2 \text{ g}^{-1}$ respectively. The long-range order and characteristic dimensions were further confirmed with SAXS and WAXS analysis. XRD detected minor crystalline traces ascribable to anatase. Lastly, loading/elution in cuvette and QCM-D highlighted the ability of the layer to uptake/release Iopamidol, showing good chemical affinity for the intended purpose. Finally, MRI-CEST was performed at different pH levels (from 5.5 to 7.4) in order to assess the responsiveness of Iopamidol as loaded in the pores of our samples. Although Iopamidol is a promising contrast agent for this application, both the difficulties encountered in the realisation of the experiment and the novelty of CEST set up open challenges for validating the concept. As for future perspectives, further characterisation with ex vivo and in vivo tests would strengthen this study.

Keywords: Iopamidol, CEST, MRI, infections, mesoporous, titania, imaging, contrast agent.

Contents

List of Abbreviations and Acronyms	xi
List of Figures	xiii
List of Tables	xv
1 Introduction	1
1.1 Detection of infections via imaging techniques	1
1.2 The novelty of MRI-CEST	2
1.3 The purpose of this project	2
2 Materials and Methods	5
2.1 Preparation of the mesoporous titania coating	5
2.1.1 Chemical principle	5
2.1.2 Experimental preparation	6
2.2 Material characterisation	7
2.2.1 SEM - Scanning Electron Microscopy	7
2.2.2 TEM - Transmission Electron Microscopy	7
2.2.3 BET - Brunauer-Emmett-Teller Analysis	7
2.2.4 XRD - X-Ray Diffraction	8
2.2.5 XPS - X-ray Photoelectron Spectroscopy	8
2.2.6 SAXS - Small-angle X-ray Scattering	8
2.2.7 Loading and elution test in cuvette	9
2.2.8 QCM-D - Quartz Crystal Microbalance with Dissipation	11
2.3 Drug testing with MRI	12
3 Results	15
3.1 Material characterisation	15
3.1.1 Morphology characterisation: SEM and TEM	15
3.1.2 BET	17
3.1.3 XRD	19
3.1.4 XPS	19
3.1.5 SAXS	22
3.1.6 Drug uptake and release	24
3.1.6.1 Loading and elution test in cuvette	24
3.1.6.2 QCM-D	25
3.2 Drug testing with MRI - first approach	27
4 Discussion	29
5 Conclusion	31
5.1 General considerations	31
5.2 Future perspectives and ideas	31
Bibliography	33
A Appendix A: Gel preparation for MRI	I

List of Abbreviations and Acronyms

For a correct and fluent interpretation of the document, here is presented a clarification of all the relevant abbreviations used in this Master's Thesis.

^{18}F -FDG PET	FluoroDeoxyGlucose Positron Emission Tomography
MRI	Magnetic Resonance Imaging
CEST	Chemical Exchange Saturation Transfer
TiO_2	Titanium dioxide (Titania)
NMR	Nuclear Magnetic Resonance
EISA	Evaporation Induced Self-Assembly
CMC	Critical Micelle Concentration
TBOT	Tetrabutyl Orthotitanate (other name for Titanium (IV) Buthoxide)
HCl	Hydrochloric Acid
SiO_2	Silicon Dioxide (Silica)
SDS	Sodium Dodecyl Sulfate
PBS	Phosphate Buffer Saline
RT	Room Temperature
STP	Standard Temperature and Pressure
EO_xPO_y	$-\text{[Ethylene Oxide]}_x-\text{[Propylene Oxide]}_y-$
PLA	Polylactic Acid
SEM	Scanning Electron Microscopy
TEM	Transmission Electron Microscopy
BET	Brunauer-Emmett-Teller
BJH	Barrett-Joyner-Halenda
SAXS	Small-Angle X-ray Scattering
WAXS	Wide-Angle X-ray Scattering
XPS	X-ray Photoelectron Spectroscopy
QCM-D	Quartz Crystal Microbalance with Dissipation
$\text{Na}_2\text{HPO}_4 \cdot 7\text{H}_2\text{O}$	Sodium Phosphate Dibasic Heptahydrate
$\text{NaH}_2\text{PO}_4 \cdot 2\text{H}_2\text{O}$	Sodium Phosphate Monobasic Dihydrate

List of Figures

1.1	Chemical structure of Iopamidol. MW = 777.09 g mol ⁻¹ . Source: https://www.adooq.com/iopamidol.html	3
1.2	NMR survey from literature. Source: [7].	3
2.1	Schematic for the Evaporation Induced Self-Assembly mechanism. Source: https://www.researchgate.net	5
2.2	Chemical representation of Titanium (IV) butoxide (TBOT), used as the inorganic precursor in this project. Source: https://www.sigmaaldrich.com	6
2.3	Standard curve prepared for concentration values ranging from 200 μM to 12.5 μM. The slope is equal to 0.0289 and the R ² value expresses a high linearity in the relation between absorbance and concentration as theorised by the Lambert-Beer's law.	9
2.4	Picture showing the setup for the loading-elution test.	10
2.5	Setup for the QCM-D test. The leftmost apparatus is the pump required to draw solution into the chambers containing the sensors. A pumping speed of 100 μl/min for the initial rinsing with PBS is displayed. The chambers on the right contain the sensors (Ti for blue and green, non-coated ; SiO ₂ for red and yellow, coated), connected to the source (either PBS or Iopamidol stock solution).	12
2.6	Representation of the setup for the experiment. Vials 1–5 are going to contain loaded glass slides dipped in gel at pH 5.5, 6.0, 6.5, 7.0 and 7.4 respectively. Vials 6–8 are going to contain coated-only slides dipped in gel at pH 5.5, 6.5, 7.4 respectively. Three more vials (here not displayed) are meant to contain gel and drug only.	12
3.1	SEM image confirming the mesoporous structure of the titania film produced. At a first glance, the pore size distribution looks narrow and the pores are nestled with no preferential order across the portion of the examined sample.	15
3.2	SEM image acquired to provide an estimation of the thickness of the mesoporous layer.	16
3.3	Two images acquired with TEM are reported here. A mesoporous randomly-ordered structure is observable at moderate magnification in 3.3a. A mild form of crystallisation can be spotted at high magnification in 3.3b.	17
3.4	BET test performed on the titania powder. The hysteresis loop formed between the adsorption and desorption curves is highlighted in the central box. For completeness, the pore size distribution obtained with the BJH desorption isotherm is presented. The characteristic peak corresponds to 33.13 Å.	18

3.5	XRD test results performed on titania powder. The red vertical lines represent the experimental values found in database for a pure reference sample of tetragonal phase (anatase).	19
3.6	XPS spectrum for the loaded sample. The plot represents the counts per second detected for binding energies ranging from 0 to 1100 eV. Major peaks detected for C1s, O1s and Ti2p. In addition to that, a small presence of N1s is observed.	20
3.7	XPS spectrum for the non-loaded sample. The plot represents the counts per second detected for binding energies ranging from 0 to 1100 eV. Major peaks detected for C1s, O1s and Ti2p. There is a minor contribution of Na1s, P2p, Cl2p, K2p and N1s.	21
3.8	Comparison of the carbon region for the two examined samples. The curves are plotted as a magnification of the full spectra.	22
3.9	X-ray scattering plot highlighting both the SAXS (purple curve) and WAXS (light-orange curve) contribution in the range $q = 0.005 - 0.5 \text{ \AA}^{-1}$. The * symbol highlights the characteristic bump, occurring at a q-value $q = 0.05433 \text{ \AA}^{-1}$	23
3.10	Scattering pattern revealed on the detection window during SAXS run. . .	23
3.11	Resulting plots from two distinct runs of the elution test. Both curves show the average reading coming from the respectively examined cuvettes. No significant changes in the trend were detected after 8 hours from the beginning of the test for the orange curve, hinting that the concentration of the bulk settled to the value of 13.7 \mu M . The second run focuses on long-term evolution and eventually settles at 12.03 \mu M after 50.25 hours. .	25
3.12	Plots of mass corresponding to the four sensors used for QCM-D. The shift in frequency has been converted to shift in mass according to equation 2.4. A vertical black dashed line is shown to separate the loading region (left) from the elution region (right). Ti-1 and Ti-2 refer to the control non-coated samples.	26
3.13	Cross-section of an examined glass slide (loaded and dipped in the gel at $\text{pH} = 7.4$).	27

List of Tables

2.1	List of the detected frequencies for Ti and TiO ₂ -coated QCM-D sensors. The fundamental is nearly 5 MHz for all of them.	11
3.1	Chemical composition (atomic %) of the examined samples.	20
3.2	Loading readings. The absorbance value (first line of each cell) corresponds to a 20-times diluted drop coming from the bulk of the cuvette. The corresponding actual concentration is presented in brackets expressed in μM. * The stock value was measured at the beginning of the loading test as a "0 h" reference value.	24
A.1	Preparation steps followed for the buffers used for the MRI test.	I

1. Introduction

1.1 Detection of infections via imaging techniques

The role of this section is to provide a deep and thorough overview of the state-of-the-art with respect to the modern techniques harnessed to detect ongoing infections on prosthetic grafts.

With the expansion of arthroplasty in orthopaedics as standard approach for addressing joint failure in lower limbs, assuring an efficient performance of the prosthetic device across its whole life-span is of utmost importance. However, despite the substantial effort put into implant designing and surgical approach for grafting over the past decades, the risks associated to the operation are still a major cause of failure: a vast epidemiologic study [1] showed that the most common causes of revision total hip arthroplasty were instability/dislocation (22.5%), mechanical loosening (19.7%) and infection (14.8%). Specifically, infection was by far the most relevant cause for prosthesis removal (74.3%) [1]. Although infections occur as frequently as 1-4%, the impact dramatically rises after revision [2] resulting in pain and subsequent failure. Whereas loosening and mechanical instability are inherently linked to the success of the design and surgeon's dexterity, infections are a consequence of the chemical environment established on the interface tissue/biomaterial. However, a common dilemma is distinguishing between aseptic and septic conditions [2, 3, 5], since in many cases infections outbreak in conjunction with mechanical loosening. Nevertheless, it is evident that they play a crucial role and their impact is to be minimised. For this purpose, a lot of interest is growing around early detection routes.

Nuclear imaging techniques such as ^{68}Ga Gallium scintigraphy, ^{111}In Indium-labeled white blood cell scanning and, more recently, ^{18}F -FDG PET have proved to be the golden standards for early infection detection [2, 3, 4].

Gallium scan was first introduced in the 70s [2] as a radionuclide imaging modality to enhance bone scintigraphy [5]. However, inherent drawbacks of ^{68}Ga and ^{67}Ga -citrate, like poor sensitivity (38%), high radiation dose and low specificity (Gallium salts accumulate not only in infection sites, but also in periosteal bone formation and aseptic loosening), made it quite obsolete with respect to other currently available approaches [2, 5].

^{111}In Indium-labeled WBC has found widespread consensus and has been deemed an excellent technique by many studies, including diagnosis for vascular grafts [2, 3, 4, 5]. The considerable advantages are high specificity, sensitivity and accuracy at expenses of some severe downsides like time and cost: white blood cells are removed from the patient, incubated with the radiopharmaceutical and reinjected back, with possible exposure to bacterial contamination in the process [2, 3].

^{18}F -FDG PET consists in constructing a representation of the tissues of interest based on the spontaneous β -decay of a 18-F-marked glucose bolus injected in the bloodstream [6]. The substance accumulates in the presence of high glycolytic active cells, among

which neutrophils and activated macrophages, thus highlighting inflammatory response and infections [2]. This technique offers good spatial resolution and relatively fast analysis, but it lacks of specificity for infections (for example, tumorous cells are glucose-demanding as well), shows artifacts due to metallic implants and is expensive and scarcely available [5].

1.2 The novelty of MRI-CEST

The success of MRI in modern clinical applications stems from its excellent anatomical resolution, soft-tissue contrast, safety and noninvasive nature [7, 8, 10]. The development of a novel contrast agent (CA) that allows reporting pH levels, metabolic activity or oxygenation content, would result in an enhancement of MRI, adding a functional analysis on top of the morphological one. For this reason, some research studies made efforts to produce Gd(III)-based complexes or H^{13}CO_2 that exhibit pH-dependent relaxivity at suitable frequencies [7]. However, the scarce spatial resolution and high cost of these approaches pushed to find a new route.

CEST (Chemical Exchange Saturation Transfer) is a recent contrast strategy for MRI. It is based on the saturation of labile proton pools at specific radiofrequencies, which are subsequently exchanged with the surrounding water molecules in the tissues. This phenomenon results in a decreased contribution from the bulk water signal, thus acting as CA [7, 8]. One of the advantages is that the labelling of mobile protons is frequency-selective, therefore the signal can be interpreted via a ratiometric approach [7, 9]. Different studies have proved the validity of CEST both *in vivo* and *in vitro*. Zhou et al. identified ischemic brain regions thanks to the difference in pH between healthy and unhealthy portions of the tissue [11]. Longo et al. published two studies to assess kidney diseases in healthy mice with pH-dependent MRI-CEST at high magnetic fields [7, 9].

1.3 The purpose of this project

The scope of this Master's thesis embraces this wide and forward-looking research scenario. The goal is to give a significant contribution in early infection detection via MRI-CEST for biomedical applications. The most important etiologic agents of prosthetic joints infections (PJI) are staphylococci [12] (54%; both *Staphylococcus aureus* and *Staphylococcus epidermidis*), even when infection is of dental origin [13]. After a first bacterial attachment onto the implant surface mediated by weak electrostatic interactions, staphylococci adhere firmly by secreting adhesins and exopolysaccharidic biofilms [12]. As a consequence of this, the pH level may locally drop from physiologic 7.4 down to more acidic values. This is the main reason why we are interested in assessing pH responsiveness of a suitable CA. With the aid of MRI, we would yield a complete and intuitive map of the prosthetic device, where unhealthy spots and anomalous pH levels would be highlighted by specific hues.

Iopamidol (Fig. 1.1) has been extensively used as CA in several CEST studies because

of its many amide and hydroxyl functional groups. It even found applications in X-Ray imaging thanks to its iodine atoms [7]. Therefore, due to the wide consensus it has found in medical applications, Iopamidol was selected as drug for our MRI tests. The expected durability of the CA inside the pores would only allow for investigations in the first weeks after implantation (where the risk of infection is higher). However, this work aims to propose a proof of concept for the feasibility of this strategy and every other consideration may be formulated only after substantial *in vivo* and *ex vivo* characterisation.

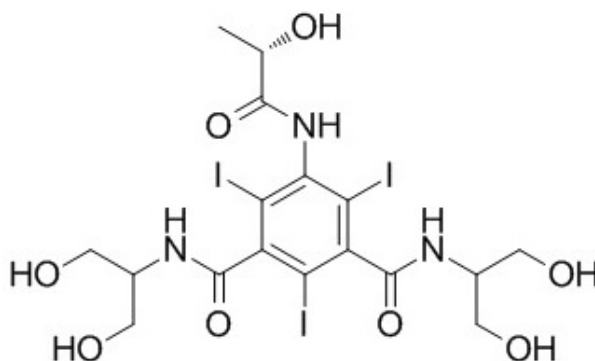


Figure 1.1: Chemical structure of Iopamidol. MW = 777.09 g mol⁻¹.

In order to characterise the responsiveness of Iopamidol (*i.e.* *saturation transfer*) a NMR test is required. As per what emerges from literature, the amide groups of Iopamidol have a much lower exchange rate with respect to the hydroxyl protons, thus being more easily detectable even by using lower magnetic fields [7]. The spectra found in their study is reported in Fig. 1.2 and commented below.

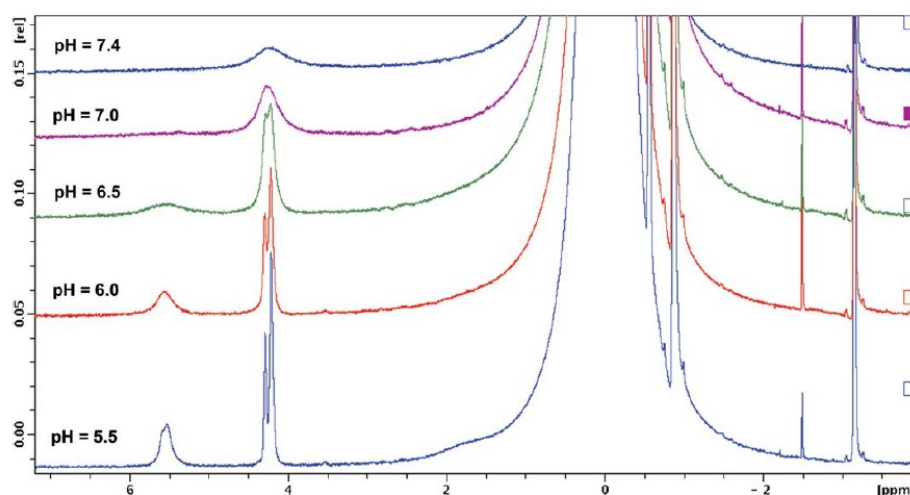


FIG. 2. High-resolution ¹H-NMR spectra (without water suppression) of Iopamidol in aqueous solution ([Iopamidol] = 200 mM, T = 308 K, B₀ = 14 T) in the pH range between 5.5 and 7.4. Chemical shifts (δ) are relative to the resonance frequency of water (δ = 0 ppm). The amide protons show multiple resonances centered at 4.2 and 5.5 ppm due to the presence of slowly interconverting conformers. [Color figure can be viewed in the online issue, which is available at wileyonlinelibrary.com.]

Figure 1.2: NMR survey from literature. Source: [7].

From the spectra, it seems evident that Iopamidol exhibits a pH-dependent response. The resonance peaks ascribable to amide groups at 5.5 ppm and 4.2 ppm get sharper as pH decreases due the decrease in exchange rate. Furthermore, the exchange rate at 4.2 ppm is lower than the one at 5.5 ppm for every pH measured (*i.e.* lower constant of exchange). This is visible from the broader peaks found at 5.5 ppm for each curve and it highlights the frequency-dependent response of Iopamidol [7]. The survey reported here was crucial for understanding the key-characteristic of the drug and further motivated our selection of Iopamidol for our tests.

Saturation transfer is calculated with equation 1.1:

$$ST = \frac{S^{-\Delta\omega} - S^{+\Delta\omega}}{S_0} \quad (1.1)$$

Taken from [8], which appears to be the most solid study on this technique. $\Delta\omega$ refers to the proton frequency shift from water resonance, $S^{\pm\Delta\omega}$ is the signal acquired at $\pm\Delta\omega$ respectively. S_0 is the control signal coming from water with no radiofrequency. Saturation transfer is further processed in the formulation of a ratiometric index (1.2) where RF_1 and RF_2 are two different RF powers.

$$RI = \frac{[(1 - ST)/ST]_{RF_1}}{[(1 - ST)/ST]_{RF_2}} \quad (1.2)$$

The elaboration of RI eventually corresponds to the wanted signal interpretation and eventually leads to image construction.

Mesoporous titania coatings are well-established materials for prosthesis functionalisation that have found their major applications for drug-delivery [14] and osseointegration [15, 19]. Their self-assembled structure is crucial for their high specific surface area and porosity, which could be harnessed for efficiently carrying functional chemicals as well as for enhanced integration with the bone [15]. For our project, this class of materials was deemed ideal for hosting Iopamidol without compromising the desirable biocompatibility and structural integrity of the prosthesis. We claim *a priori* that there should be a good interaction between the mesoporous film and the drug, which is expected to adhere either chemically or by physically adsorption. Our work will involve extensive material characterisation (featuring investigation on structure, morphology, chemical composition, specific surface area and drug uptake/release) together with an *in vitro* study for validation of our strategy with MRI.

2. Materials and Methods

This chapter aims to provide a thorough description of the materials and methods used in this project. All of the chemicals present were purchased from Sigma-Aldrich. For the sake of readability, layer characterisation and MRI testing are presented in separate sections.

2.1 Preparation of the mesoporous titania coating

2.1.1 Chemical principle

The key-strategy of this step is the EISA method (*Evaporation Induced Self-Assembly*). A self-assembly method is defined as a process in which a material spontaneously organises through non-covalent interactions with no external intervention [16]. This is achieved by using a surfactant as a templating agent, dispersed in a solution of the desired inorganic precursor (see Fig. 2.1), with concentration $C \ll \text{CMC}$. The latter typically consists of a liquid phase wherein a metallic atom (*e.g.* Ti, like in our case) coordinates organic oxidised side-groups, later cleaved via stirring with a strong acid to enable the network formation (sol \rightarrow gel transition). The role of the surfactant becomes clear when considering the micelle formation phenomenon. As the solvent, usually a volatile chemical, undergoes preferential evaporation during the coating process, the surfactant becomes more and more concentrated, crossing the critical micelle concentration. This, in turn, promotes the organisation of the surfactant in spherical (or cylindrical) packages, wherein the hydrophobic side of the chain is shielded in the core and the hydrophilic head is exposed to the bulk of the solution [16]. The result is a hybrid mesostructure with a random distribution of organic agglomerates nestled in an inorganic gel. Finally, a heat treatment (*i.e.* calcination) provides the removal of surfactants, leaving a mesoporous material (typical pore width ranging from 1 nm to 10 nm) as they are gradually burnt away from the sample.

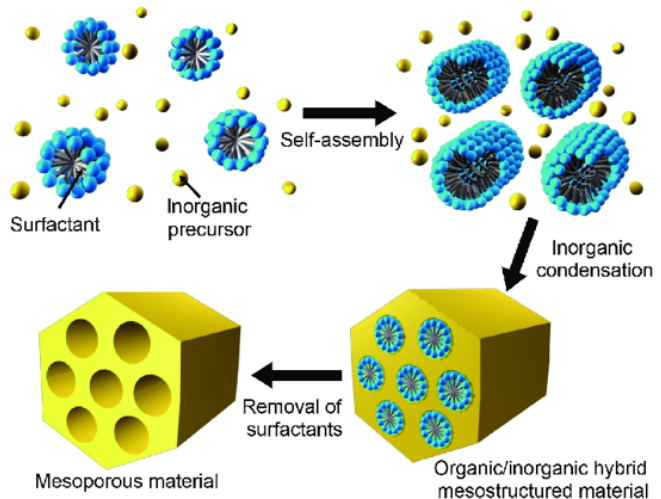


Figure 2.1: Schematic for the Evaporation Induced Self-Assembly mechanism.

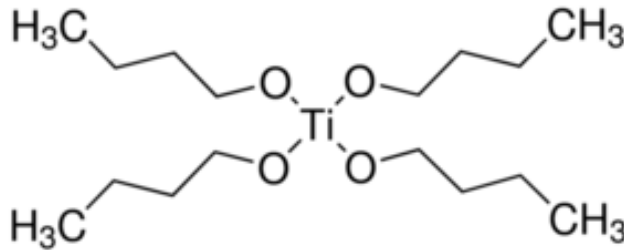


Figure 2.2: Chemical representation of Titanium (IV) butoxide (TBOT), used as the inorganic precursor in this project.

2.1.2 Experimental preparation

The experimental procedure adopted in this work is as follows: the precursor solution was prepared by adding 1.6 g of HCl (37 wt.%) to 3.13 g of Titanium (IV) butoxide (97 %) (chemical structure reported in Fig. 2.2) under vigorous stirring for 3 hours until homogeneous, meaning that the cleavage of the side-groups has occurred. A second solution containing 0.5 g of Pluronic[®] P123 (triblock copolymer $\text{EO}_{20}\text{PO}_{70}\text{EO}_{20}$) and 8.5 g of ethanol (99.5 %) was left to stir and added to the precursor solution thereafter. A similar protocol has been found in literature [17].

The layer was deposited on glass slides (large: 55x26 mm² and small: 35x9 mm²) as well as silicon wafers (15x15 mm²) via dip-coating (speed: 1 mm/s). QCM-D sensors (Qsx-303 SiO₂ and Qsx-310 Ti, Biolin Scientific AB) were coated via spin-coating (7000 rpm; 2100 rps²; 60 s, 50 μl of solution used per sample) for the QCM-D test (refer to Section 2.2.8 and Section 3.1.6.2). Before proceeding with calcination, every sample was left overnight in a plastic container to achieve a complete self-assembly with no possible contamination by external agents. All the surfaces available were extensively cleaned before depositing the layer, in order to achieve good wetting as well as to contain the presence of impurities that could negatively affect the results. In the case of simple glass slides, the cleaning consisted in two cycles of ultrasonication: the first with a solution of Sodium Dodecyl Sulfate in Milli-Q water (SDS, 2 wt.%) for 10 minutes at room temperature, the second with pure Milli-Q water (18.2 M Ω ·cm) in analogous conditions. The silicon wafers were cleaned through Piranha solution (5:1:1 Milli-Q water : NH₄OH : H₂O₂ ratio) for 15 minutes at 80 °C, prior UV treatment for 1 hour.

In order to complete the procedure, all the samples studied in this project underwent the same heat treatment in a calcination oven (Nabertherm, Wilhelm Tham AB). The surfactant was successfully removed with a first gradual heating ramp (1 °C/min from RT up to 350 °C) followed by a 4 hours-long plateau at 350 °C and a natural cooling down to room temperature. The temperature was chosen as to ease the thermal degradation of the organic species without altering the titania significantly, namely avoiding undesired crystallisation phenomena. Furthermore, the mild heating-up ramp guaranteed that no intense thermal stresses arose around the pores or across the thickness of the sample. In addition to that, the calcination of Pluronic[®] micelles was assured to be even and gradual. Every sample was preserved in suitable plastic containers under N₂ atmosphere to prevent

contamination.

Some of the performed characterisation tests required a sample in the powder form (*i.e.* BET analysis, TEM, SAXS and XRD). For this reason, a total of 83 mg of mesoporous titania powder was produced by scraping the calcinated film off glass slides.

For all the tests that required a loading step with the drug, a Iopamidol (1 mg/ml or, equivalently, 1.29 mM) in PBS (0.01 M, pH 7.4 at 25°C) was prepared.

2.2 Material characterisation

2.2.1 SEM - Scanning Electron Microscopy

A Leo Ultra 55 electron microscope (Carl Zeiss Meditec AG, Oberkochen, Germany) operating at 20.00 kV with magnification up to x400.00k was used to visually investigate the morphology and the structure of the as-calcinated mesoporous film applied to silicon wafers. Due to the conductivity of the substrate, sputter coating was not required, and moreover it would have been detrimental for the pores present on the surface. This test was conducted in order to have a first glance on the pore size and distribution as well as layer thickness.

2.2.2 TEM - Transmission Electron Microscopy

A FEI Tecnai T20 TEM/STEM operating at 200 kV with a LaB6 was used to expand the visual characterisation of the mesoporous film. A sufficient amount of powder was mixed with ethanol and applied on 3 mm diameter discs for the microscope. The magnification scale applied to acquire images ranged from x29k to x285k.

2.2.3 BET - Brunauer-Emmett-Teller Analysis

BET isotherm is a widespread analysis that provides measurement of useful parameters, such as specific surface area, pore size distribution as well as adsorption-desorption phenomena for mesoporous materials [20]. The rationale for the choice of this test in our project lies in assessing the aforementioned key-quantities for the material of interest, so as to further characterise it. The pore size and distribution play an important role for the uptake-release kinetics of Iopamidol, in conjunction with specific surface area, which is an indication of reactivity of the film.

According to the standard BET theory, the linear form of the isotherm can be expressed by the following equation:

$$y = \frac{x}{q \cdot (1 - x)} = \frac{1}{q_m \cdot c} + \left(\frac{c - 1}{q_m \cdot c} \right) \cdot x \quad (2.1)$$

where $x = P/P_0$ expresses the ratio of the partial pressure of the adsorbate to its saturation

partial pressure at the system temperature, c is the BET constant, q_m is the absorbed gas quantity at STP to produce an apparent monolayer on the surface of the sample, and q is the absorbed gas quantity at STP [20]. These parameters can be easily extrapolated from the linear regression of the adsorption isotherm in the range $0.05 < x < 0.35$ and can be further utilised to calculate the specific surface area (*i.e.* total surface area divided by the mass of the sample).

A Micromeritics TriStar 3000, Chemical Instruments AB was used for the experiment. The BET analysis was executed on 77.7 mg of mesoporous titania powder produced as described in Section 2.1.2. Prior to the experiment, moisture was eliminated via N₂ blowing and heating (1 hour at 90 °C + 4.5 hours at 350 °C), thus resulting in 71.1 mg dry weight. A sample of Silica-Alumina with known specific surface area and pore size ($200 \pm 6 \text{ m}^2 \text{ g}^{-1}$ and $112 \pm 15 \text{ \AA}$ respectively) was chosen as a reference for the reading and underwent the same heating program as the titania powder.

The powder turned from being pale white to grey ash, hinting that some crystallisation phenomena have been triggered while executing the test, as confirmed by the XRD test.

2.2.4 XRD - X-Ray Diffraction

The goal of the XRD test is to investigate over the possible crystalline nature of the sample. The powder is bombarded with X-rays originated from an X-ray tube. The source of X-ray works according to the well known principle of electrons extracted via thermionic effect and accelerated toward a target window by applying a voltage. As the radiation hits the sample, it produces diffraction, that is constructive interference in preferred directions where Bragg's law holds [21]. This analysis provides data on the crystalline species present in the powder, degree of crystallinity and lattice parameters. A Bruker D8 advance (Bruker Corporation, Billerica, MA, USA) with a radiation wavelength of 1.5405 \AA (Cu K α 1 radiation) was used for this project. The analysed angles covered a range 2θ scanning range of $20\text{--}60^\circ$, with a step size of 0.05° .

2.2.5 XPS - X-ray Photoelectron Spectroscopy

The goal for this test is to investigate on the chemical composition (atomic %) of the produced mesoporous layer. For a more complete survey, in this project we examined two samples produced on Silicon wafers: the first was coated only, while the second underwent loading with the Iopamidol solution for about 2 days. A Versa Probe III - Scanning XPS Microprobe, Physical Electronics was used for this experiment. The machine uses a monochromatic X-ray source Al K α (1486.6 eV), with a beam size $100 \text{ }\mu\text{m}$. The analysed area was $400 \times 500 \text{ }\mu\text{m}^2$ with a depth of approximately 5 nm .

2.2.6 SAXS - Small-angle X-ray Scattering

The SAXS test was performed on the sample in order to get information about the structure and long-range order of the mesoporous titania. The small-angle X-ray scattering

experiment was performed with the aid of a SAXSLAB Mat:Nordic with detector distance of 1081 mm for SAXS and 131 mm for WAXS with a beam size of 0.3 mm. The data were collected on a Pilatus 300k single-photon counter from Dectris. The wavelength of the used X-ray beam was 1.54 Å produced by a Rigaku 003 X-ray Microfocus Cu-Radiation source. The q -values, defined in 2.2, were collected in the range 0.005–0.075 Å⁻¹ for SAXS, carried out for 1800 s for improved quality of the signal. For the sake of completeness, an additional WAXS (for 300 s) analysis was performed in the q -range 0.0075–0.5 Å⁻¹.

$$q = 4\pi \cdot \frac{\sin\theta}{\lambda} \quad (2.2)$$

Where q is the momentum transfer in the reciprocal-space [Å⁻¹], θ is the scattering angle [rad] and λ the wavelength of the radiation [Å⁻¹].

For the data analysis, any noise coming from the glass capillary containing the powder was filtered out and the curves were smoothed with an average moving filter operation. This allowed highlighting the general trend of the curve together with the relevant bumps observed.

2.2.7 Loading and elution test in cuvette

This test was essential to shed light on the general behaviour of our mesoporous layer in the presence of a solution containing the drug, *i.e.* Iopamidol, with respect to uptake and release kinetics.

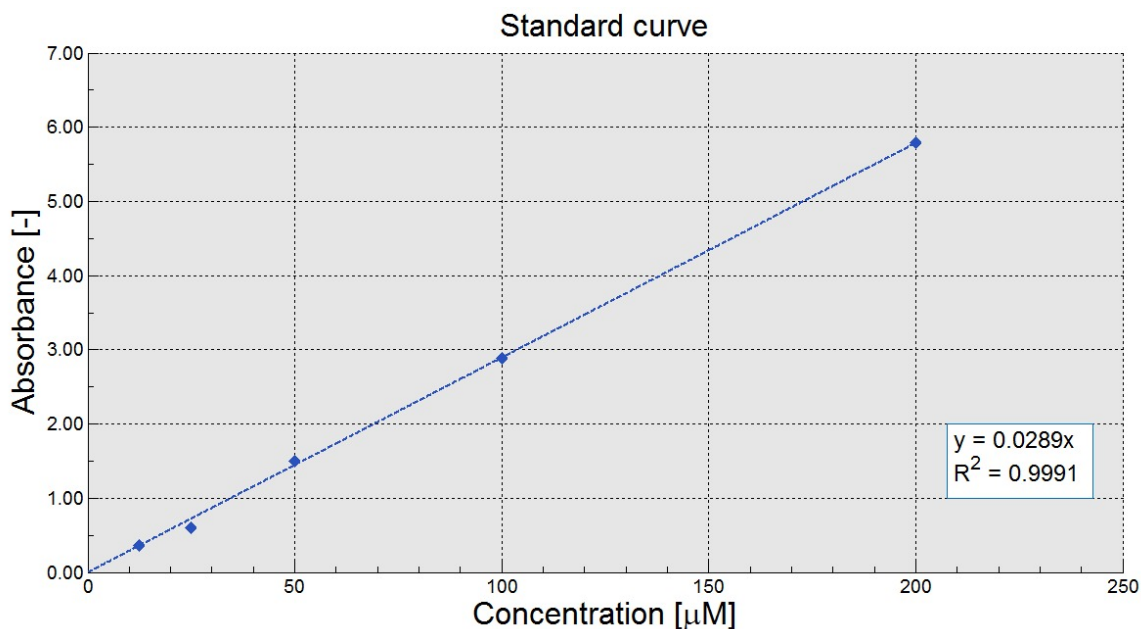


Figure 2.3: Standard curve prepared for concentration values ranging from 200 µM to 12.5 µM. The slope is equal to 0.0289 and the R^2 value expresses a high linearity in the relation between absorbance and concentration as theorised by the Lambert-Beer's law.

2. Materials and Methods

The idea is to first load the coated slides with a solution containing the drug, and subsequently place them in a blank solution to trigger the elution. During both the steps, concentration readings were taken with a ThermoScientific NanoDrop One^C machine until it was likely that the bulk had settled. For this purpose, a standard curve describing Lambert-Beer's law (2.3) was prepared, taking into account that the characteristic peak of absorbance of the drug occurs at a wavelength $\lambda = 243$ nm (shown below in Fig. 2.3).

$$A = \epsilon_{\lambda} \cdot l \cdot C \quad (2.3)$$

With respect to the curve, y corresponds to the Absorbance (A), x is the concentration (C) expressed in μM , and the slope results from the product between the molar attenuation coefficient and the path length ($\epsilon_{\lambda} \cdot l$).

An array of six small glass slides was coated with a mesoporous titania film as per described in Section 2.1.2, subsequently held on a conveniently 3D-printed PLA support and deposited in a cuvette (nominal volume 4.5 ml), as shown in Fig. 2.4. A Phosphate Buffer Saline (PBS, 0.01M, pH 7.4 at 25 °C) was prepared and used for the subsequent steps. The cuvette was first loaded with 3.3 ml of a solution of Iopamidol in PBS (1 mg/ml) for the required amount of time.

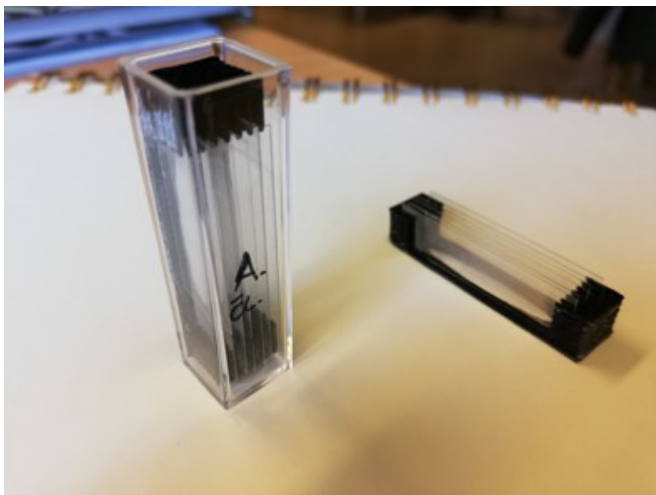


Figure 2.4: Picture showing the setup for the loading-elution test.

The readings taken during the loading, needed to be diluted by a factor 20 in order for them to fall in the standardisation range. The whole setup was rinsed in PBS for a given amount of time, short enough to get rid of the excess of Iopamidol solution wetting the structure without triggering premature elution of the drug from the pores. This step was preliminary to the elution phase of the experiment, where the main focus is observing the way the drug diffuses in the bulk from the loaded pores. The elution took place in a distinct cuvette containing the setup and 3.3 ml of PBS.

A blank test on the support only was performed with the intention of establishing whether the polymeric nature of the support could affect the results negatively by absorbing the drug preferentially. Every step of the test was executed at room temperature and making sure that no evaporation of the PBS occurred during the whole experiment. For this purpose, the cuvettes were sealed tightly with an aluminium foil. For a more solid dataset, two cuvettes per run were examined simultaneously and triple readings for each cuvette were taken and subsequently averaged. Further discussion on the results is presented in Section 3.1.6.1.

2.2.8 QCM-D - Quartz Crystal Microbalance with Dissipation

QCM-D was performed at $T = 22\text{ }^{\circ}\text{C}$ on four distinct sensors in order to consolidate the analysis on the drug uptake-release pitched with the test in cuvette. Two SiO_2 sensors were coated according to the spin-coating parameters reported in Section 2.1.2. Two extra Titanium sensors were used as control samples. Due to the spontaneous nature of titanium oxidation, it is possible that their surface exhibited a TiO_2 layer, which is however non-mesoporous. For this reason, they could offer an interesting basis for comparison with the coated sensors, as the role of the pores would be highlighted. The apparatus checked for the characteristic resonance frequencies of each sensor before the experiment: in particular, peaks corresponding to the fundamental, the 3rd, 5th and 7th overtones were detected (see Table 2.1). For all the next readings, as further discussed in Section 3.1.6.2, variations in the 3rd overtone will be taken into account. The rationale for this choice is related to the depth of analysis, which increases across the thickness with decreasing frequency. Therefore, in other words, higher overtones (at higher frequencies) would give only shallow information on the mesoporous layer, overlooking mass variation in the deeper sections of the sample.

	Fundamental (Hz)	3rd (Hz)	5th (Hz)	7th (Hz)
Ti-1	4955835	14851989	24750105	34647335
Ti-2	4955127	14851345	24748747	34645475
Coated-1	4958921	14860005	24763909	34666476
Coated-2	4956002	14851728	24750021	34646859

Table 2.1: List of the detected frequencies for Ti and TiO_2 -coated QCM-D sensors. The fundamental is nearly 5 MHz for all of them.

The samples were rinsed with PBS, pumped at 100 $\mu\text{l}/\text{min}$ for 5 minutes, to acquire an initial stable baseline. Thereafter, injection of a stock solution (Iopamidol in PBS, 1 mg/ml) was started at a pumping speed of 25 $\mu\text{l}/\text{min}$ for 10 minutes. This approach guaranteed a gradual complete replacement of the PBS volume in the system. After the initial injection and making sure that all the PBS was replaced by the stock solution, the samples were left for 24 hours of static loading until the readings in the 3rd overtone settled to a plateau. As a final step, the chambers were again rinsed with PBS to detect a possible elution process. This would be expected according to the loading/elution test performed in cuvette. This step was carried out for 6 hours. The adopted setup is presented in Fig. 2.5. The apparatus used is a four-chambers Q-Sense[®] E4 Analyzer, Biolin Scientific.

The shift in frequency Δf is linked to the change in mass Δm through Sauerbrey's equation (2.4).

$$\Delta m = -\frac{C_{\text{QCM-D}} \cdot \Delta f}{n} \quad (2.4)$$

Where $C_{\text{QCM-D}}$ is the mass sensitivity constant, taken as equal to 17.7 $\text{ng Hz}^{-1} \text{cm}^{-2}$ [22], and n is the overtone number.

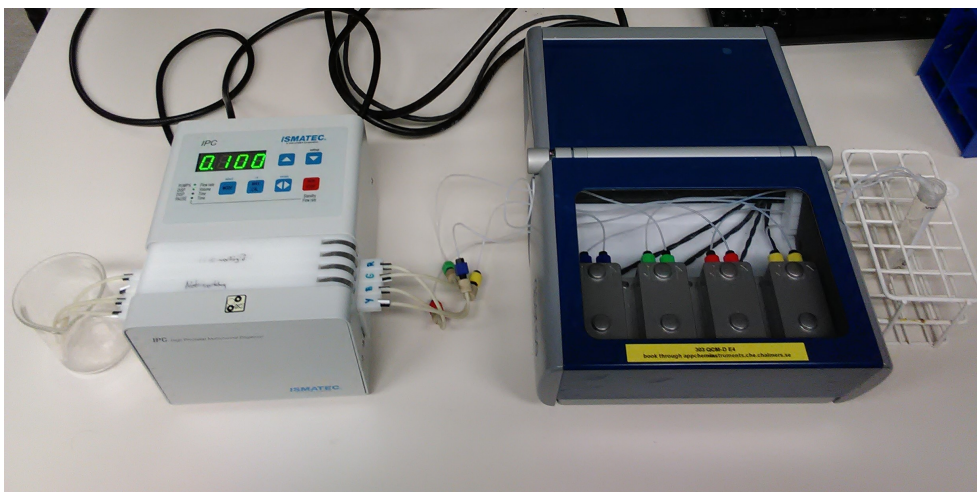


Figure 2.5: Setup for the QCM-D test. The leftmost apparatus is the pump required to draw solution into the chambers containing the sensors. A pumping speed of 100 $\mu\text{l}/\text{min}$ for the initial rinsing with PBS is displayed. The chambers on the right contain the sensors (Ti for blue and green, non-coated ; SiO_2 for red and yellow, coated), connected to the source (either PBS or Iopamidol stock solution).

2.3 Drug testing with MRI

The goal of this experiment is crucial to the whole purpose of this project, that is to establish a direct correlation between the drug of interest (*i.e.* Iopamidol) and pH via the CEST technique for magnetic resonance imaging described in Chapter 1. For this test, five glass slides ($40 \times 8 \text{ mm}^2$) were coated and loaded with a Iopamidol (1 mg/ml) in PBS (0.01M, pH 7.4 at 25 $^\circ\text{C}$) solution for three days, whereas three slides of the same size were coated only and used as control.

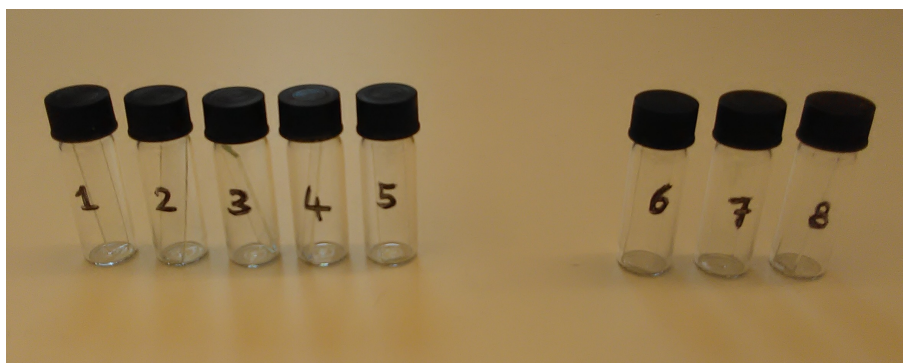


Figure 2.6: Representation of the setup for the experiment. Vials 1–5 are going to contain loaded glass slides dipped in gel at pH 5.5, 6.0, 6.5, 7.0 and 7.4 respectively. Vials 6–8 are going to contain coated-only slides dipped in gel at pH 5.5, 6.5, 7.4 respectively. Three more vials (here not displayed) are meant to contain gel and drug only.

The idea is to preserve each coated slide in a glass vial and then dip each one of them in a separate glass vial containing a gel at a specific pH value (Fig. 2.6). Three additional glass vials containing the gel and Iopamidol (30mM) without any slide were used as further control samples.

The gel was produced by using phosphate buffer saline solutions 0.1 M (thorough description of the chemicals and quantities used for the preparations available in Appendix A) at different pH levels and Lutrol[®] F127 Poloxamer 407 (triblock copolymer EO₁₀₁PO₅₆EO₁₀₁), 30% wt.

For the experiment 9.4 T MRI apparatus was used at 18 °C. Expected results from this proposed setup would be highlighting different shades corresponding to different pH levels as well as proving the concept for future experimental sessions.

3. Results

This section provides a thorough report of all the data gathered during the experimental part. The main goal is to analyse the information deriving from the tests with scientific critical sense and reflecting upon the possible flaws and practical issues encountered in the realisation of the material production and characterisation. All plots (except for XRD and XPS) and necessary calculations have been performed with Matlab®.

3.1 Material characterisation

3.1.1 Morphology characterisation: SEM and TEM

From the results deriving from the electron microscopy tests, it is possible to infer that the samples showed a convincing porous structure, as shown in Fig. 3.1 and Fig. 3.3.

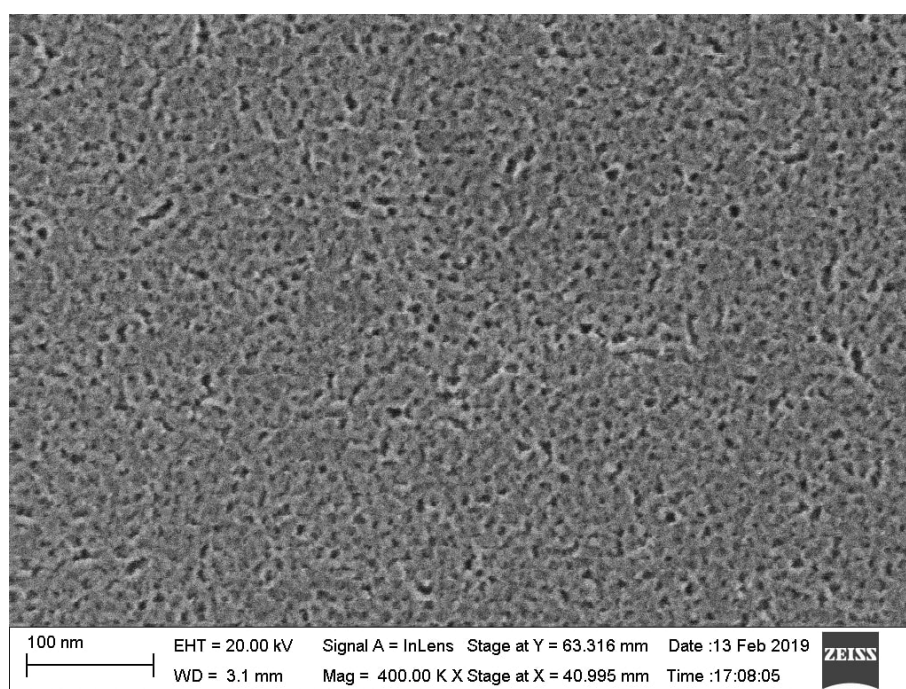


Figure 3.1: SEM image confirming the mesoporous structure of the titania film produced. At a first glance, the pore size distribution looks narrow and the pores are nestled with no preferential order across the portion of the examined sample.

During the SEM session, some image drifting phenomena due to the non-conductivity of the relatively thick titania layer were observed. As presented in Fig. 3.2, the layer was

3. Results

estimated to be as thick as ~ 200 nm. Interestingly enough, it is possible to spot some pore clusters, possibly caused by the random trajectory of the emanating surfactant micelles during calcination. As a first qualitative estimation, further confirmed by the BET test (as discussed in Section 3.1.2), the pore width appears to be in the range of 2-10 nm, thus proving the mesoporous nature of the produced material.

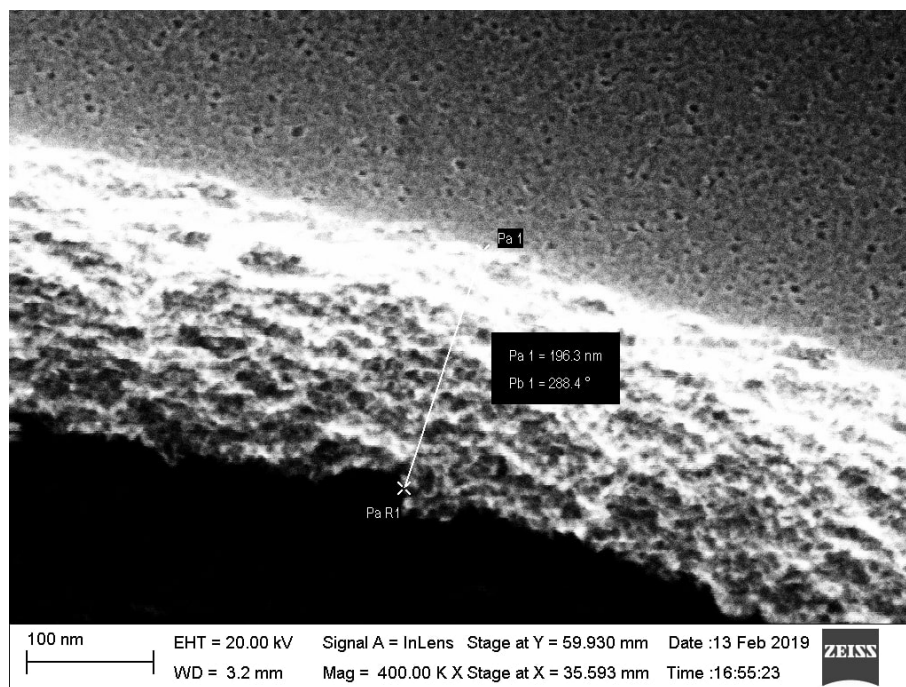
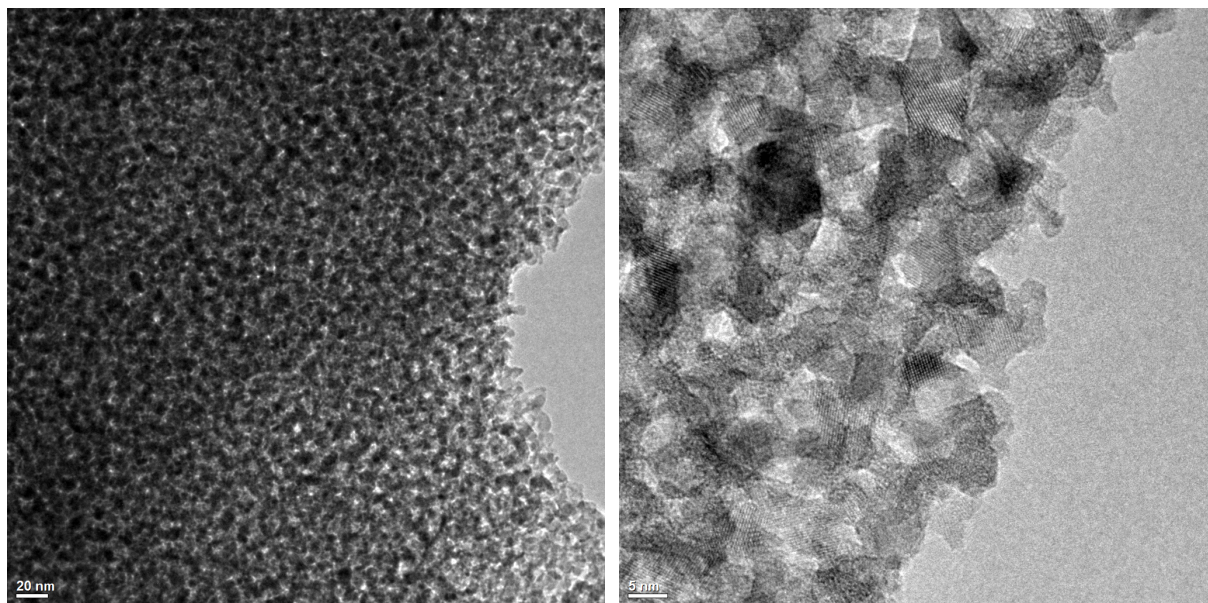


Figure 3.2: SEM image acquired to provide an estimation of the thickness of the mesoporous layer.

The TEM analysis further extends and completes what observed with SEM. The main results are reported in Fig. 3.3. Judging by the acquired images, the sample looks mainly amorphous and mesoporous. Those two characteristics are not only highly desirable but also crucial for a successful functionalisation of the biomedical implant. This becomes evident if considering that an amorphous disordered layer would allow an anisotropic drug uptake. In other words, the graft would be loaded with no preferential order, thus allowing a more homogeneous distribution of the drug across the surface and, consequently, a better and easier signal interpretation. However, during the experiment, some diffraction patterns were observed, and those correspond to minor crystalline regions spotted in the powder. As further highlighted by XRD (refer to Section 3.1.3) the crystallisation extent appears to be rather minor and circumscribed. Moreover, some of the crystals were produced directly when moving to high magnifications, due to the substantial local energy density produced by the electron beam.



(a) Magnification: x29k

(b) Magnification: x145k

Figure 3.3: Two images acquired with TEM are reported here. A mesoporous randomly-ordered structure is observable at moderate magnification in 3.3a. A mild form of crystallisation can be spotted at high magnification in 3.3b.

3.1.2 BET

Fig. 3.4 illustrates the curves of adsorption and desorption.

Many interesting results can be deduced from the BET test. IUPAC has provided a useful classification of the possible isotherms resulting from a BET test. For the following graphical considerations, refer to [23]. The general trend of the desorption (red) and adsorption (green) curves suggests a main type III behaviour, together with a hysteresis loop for relative pressure values in the range 0.4 – 0.7. The marked type III trend is ascribable to the rather high presence of glass residues deriving from the powder production process. These relatively massive shards obviously show a flat surface, with consequent poor specific surface area and non-porous texture. Therefore, N_2 simply covers the exposed glass surface with a monolayer, and the relative pressure necessary for forcing the gas into the pores of the actual mesoporous powder becomes easily overshadowed. However, the presence of a mesoporous material is clearly evident from the type-IV hysteresis loop. According to the accepted BET theory, there is a correlation between the shape of the hysteresis loop and the structure of a mesoporous material (*e.g.*, pore size distribution, pore geometry, and connectivity) [23]. The loop itself is a consequence of the capillary condensation the gas undergoes while permeating the pores of a mesoporous material: the depression needed to extract the condensed N_2 from the pores is non-symmetrical with respect to the pressure needed to infiltrate the pores. This could signify the presence of bottle-neck pores, cylindrical, slit-shaped pores or combination of the three [24]. Due to the influence of the glassy contaminants, the shape of the loop is hardly construable, but may suggest the presence of cylindrical pores with possible tracks of bottle-necks nonetheless.

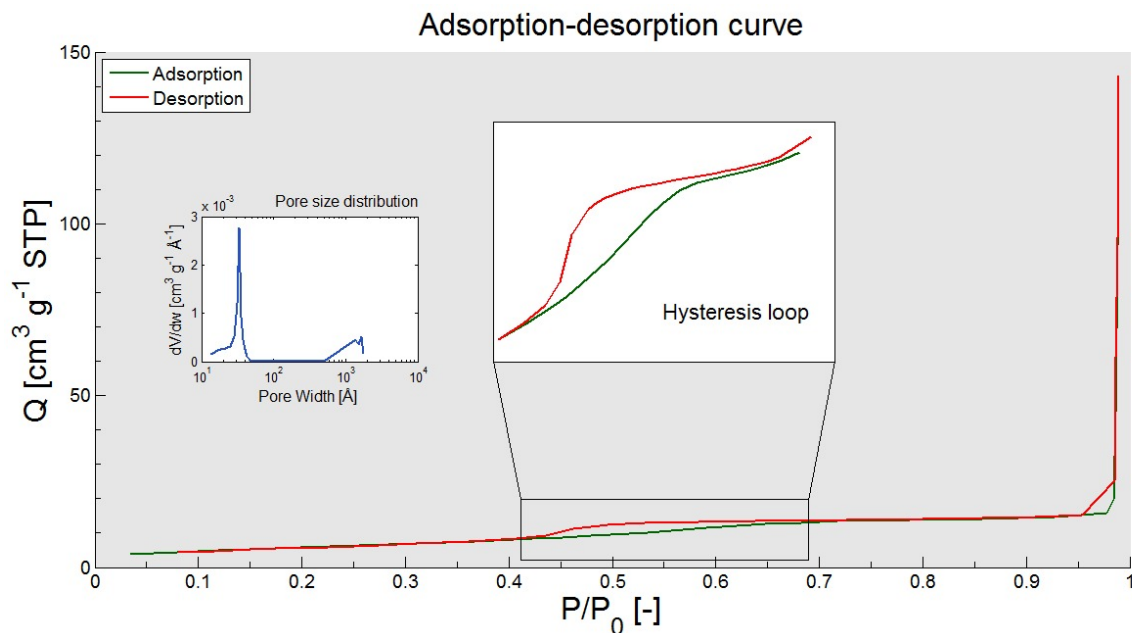


Figure 3.4: BET test performed on the titania powder. The hysteresis loop formed between the adsorption and desorption curves is highlighted in the central box. For completeness, the pore size distribution obtained with the BJH desorption isotherm is presented. The characteristic peak corresponds to 33.13 Å.

As remarkable quantitative results from the BET test, we report that the average pore size is 57.6 Å, the single-point adsorption total pore volume of pores less than 1254 Å width at $P/P_0 = 0.9843$ is $V_s = 0.031 \text{ cm}^3 \text{ g}^{-1}$, and, lastly, the specific surface area is $SA_{BET} = 21.32 \text{ m}^2 \text{ g}^{-1}$. Except for the pore width, which is logically only ascribable to the pores of the titania powder, the specific volume and specific surface area turned out to be considerably smaller than expected, at least of one order of magnitude. This consideration stems from a comparison with literature: Galkina, O. L., et al. produced a TiO_2 -P123 mesoporous film and characterised it with BET [25]. They estimated the surface area to be $105 \text{ m}^2 \text{ g}^{-1}$, and the total pore volume to be $0.328 \text{ cm}^3 \text{ g}^{-1}$. A plausible rationale for this gap may lie once again on the impurities contained in our examined sample. Hence, those two values are more appropriately to be considered as an indicative lower bound, thus hypothesising that our mesoporous material possesses better properties. Good available volume and surface area would, in fact, imply better efficiency and more free space for drug infiltration.

As a final consideration, the pore size distribution is calculated via using the BJH desorption isotherm. BJH is a procedure used for assessing pore size distribution in mesoporous samples with the help of Kelvin model for capillary condensation/evaporation [26]. The desorption branch of the BJH isotherm is generally more appreciated than the adsorption branch amongst the scientists, as the evaporation process takes place under thermodynamic equilibrium, and it is typically preferable over the adsorption branch when dealing with cylindrical pores, at expense of inaccuracy in case of bottle-neck effects [26]. It is evident from the blue plot reported in the box in Fig. 3.4 that the major contribution to

the total pore volume is originated from the pores in the mesoporous range (2-50 nm). The final ripple may be due to gas penetration in some micrometric cracks of the glass shards.

3.1.3 XRD

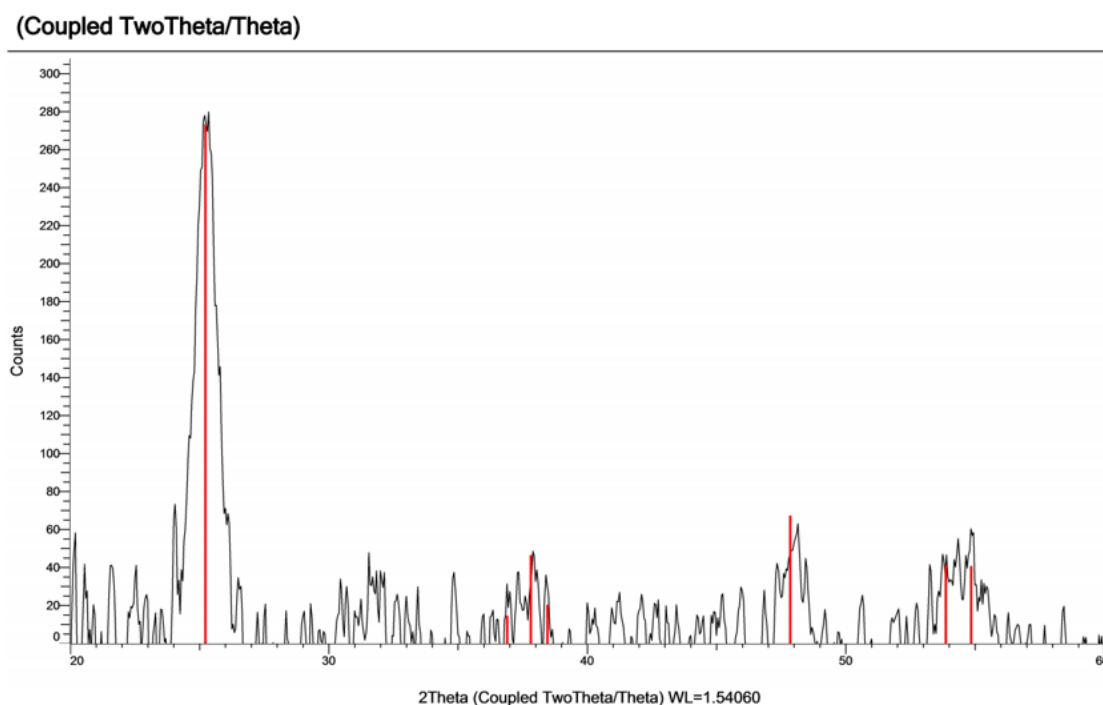


Figure 3.5: XRD test results performed on titania powder. The red vertical lines represent the experimental values found in database for a pure reference sample of tetragonal phase (anatase).

Fig. 3.5 shows the spectrum acquired from the XRD test. The raw datafile presented a huge baseline noise possibly coming from contaminants. However, the basic fingerprint of our material turned out to be matching the XRD profile of anatase-TiO₂, represented by the vertical red stems in Fig. 3.5, which in fact appears to be the dominant crystalline phase. Some minor peaks might be associated to small contributions of *rutile* or even *brookite* as per comparison with Galkina, O. L., et al. [25]. However, the detected peaks are rather wide and noisy, thus suggesting that the crystals are small and the majority of the sample exhibits an amorphous structure. This conclusion is further confirmed by other studies retrieved in the literature [17].

3.1.4 XPS

The results deriving from XPS give birth to interesting observations. Table 3.1 summarises the contribution of each element and respective orbital to the total counts detected. Fig. 3.6 and Fig. 3.7 report the survey spectra coming from the spectroscopy.

	Ti2p	O1s	C1s	N1s	Na1s	P2p	Cl2p	K2p
Non-loaded	21.20	60.20	18.12	0.48	—	—	—	—
Loaded	18.91	56.76	9.91	0.18	10.90	1.68	1.19	0.47

Table 3.1: Chemical composition (atomic %) of the examined samples.

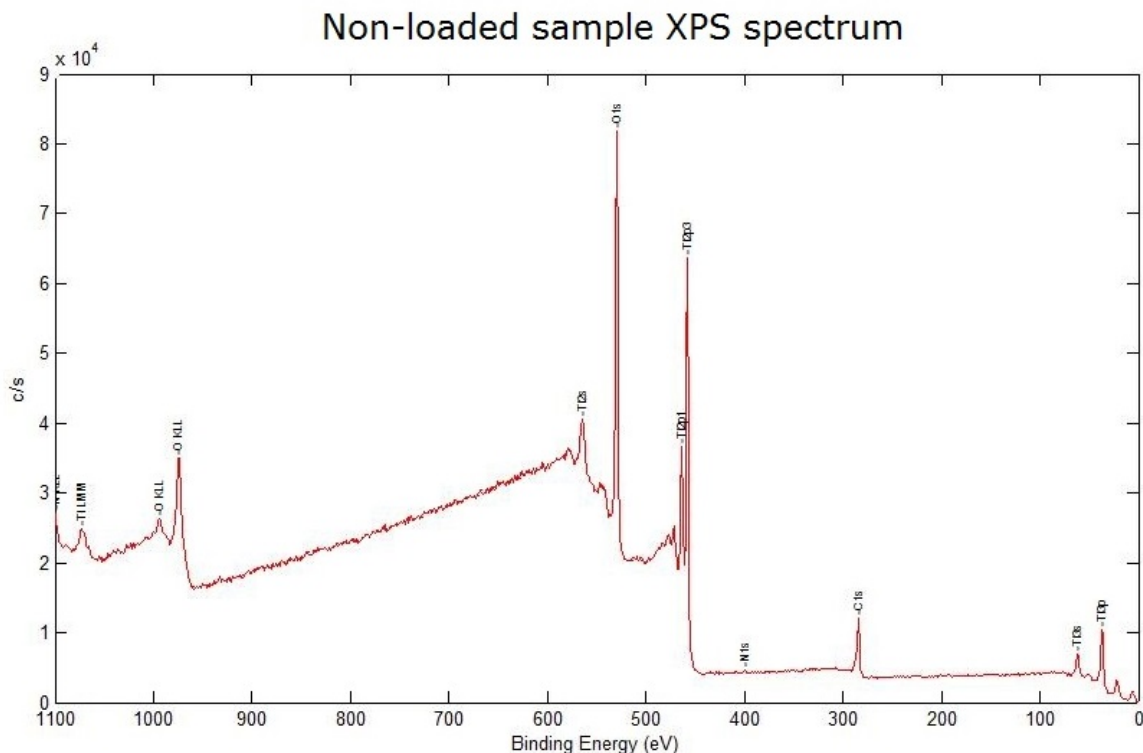


Figure 3.6: XPS spectrum for the loaded sample. The plot represents the counts per second detected for binding energies ranging from 0 to 1100 eV. Major peaks detected for C1s, O1s and Ti2p. In addition to that, a small presence of N1s is observed.

It is clearly evident that the majority of our produced sample consists of titania, thus strengthening what claimed above after the XRD test (Section 3.1.3). The non-loaded sample (see Fig. 3.6) exhibited two peaks corresponding to $Ti2p_{1/2}$ and $Ti2p_{3/2}$ (454.1 eV, with a mutual shift of $\Delta=6.17$ eV), which signifies that Ti ions lie in an octahedral environment [28, 29]. The peak for O1s at 531.0 eV is an indication of the Ti-O bond in TiO_2 , whereas no peak in the characteristic Ti-C bond domain (~ 281 eV [28, 29]) was found, meaning that the carbon contribution is fully ascribable to uncalcinated residual organic phases (*i.e.* P123 micelles). However, as presented in Fig. 3.8, the signal associated to carbon indicates the presence of different hybridisation degrees, suggesting that the moderate contribution of carbon may be also due to residual cleaved groups coming from the inorganic precursor, namely TBOT.

The loaded sample (Fig. 3.7) showed a very similar chemical composition compared to the non-loaded wafer.

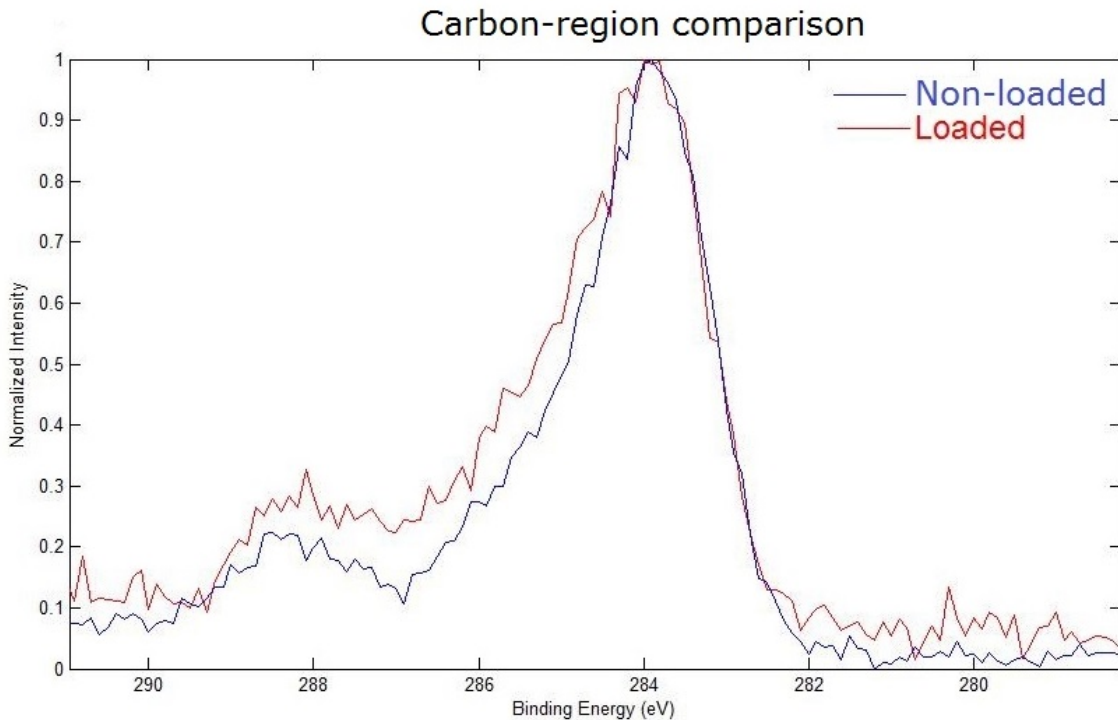


Figure 3.8: Comparison of the carbon region for the two examined samples. The curves are plotted as a magnification of the full spectra.

From Fig. 3.8, it is clear that the loaded sample presented a broader carbon contribution, coming from the overlapping of multiple hybridisation states. We detected four bands around 285 eV, each one corresponding to different carbon bonds (*i.e.* C–C, C–O, C=O/O–C–O and –O–C=O–). Despite the carbon amount being halved when compared to the non-loaded sample, this suggests that the carbon atoms lie in a different and more diverse chemical environment. This likely hints at the presence of Iopamidol, which has a complex aromatic structure. The hypothesis is further supported by the oxygen peak, which clearly differs from the non-loaded sample for the presence of =O bonds and aromatic groups. Unfortunately, despite that Iopamidol contains iodine atoms, peaks associated to C–I bond were scarcely observable. All the results reported in this section, with respect to atomic composition and peaks location, are rather consistent with several other studies on mesoporous titania films retrievable in the literature [17, 18, 19, 28, 29].

3.1.5 SAXS

From SAXS it is possible to conclude that the sample exhibited a long-range order with only one characteristic peak, marked with * in the SAXS (purple) region of the plot in Fig. 3.9. Converting the q -value at the purple bump to distance, one obtains $d^* = 115.6 \text{ \AA}$, which is most likely readable as the average pore-pore distance. Further in the examined WAXS range, no other peak was found, meaning that it was not possible to detect a symmetry in the pore distribution. However, a minor bump in the transition region (MAXS) is visible. This would correspond to a $d = \sim 6.0 \text{ nm}$, easily interpretable as a characteristic pore size.

As for the q -value at the peak, it has been shown in recent studies that it is most likely related to the pore width [17, 27]. In the matter of question, a larger pore width has an implication on the bump, which appears to shift toward smaller q -values. From a direct comparison with this study, we can conclude that the bump exhibited by our sample (MAXS) could be associated with a pore size of ~ 6.0 nm, which would confirm our claim and what derived from the BET test, reported in Section 3.1.2.

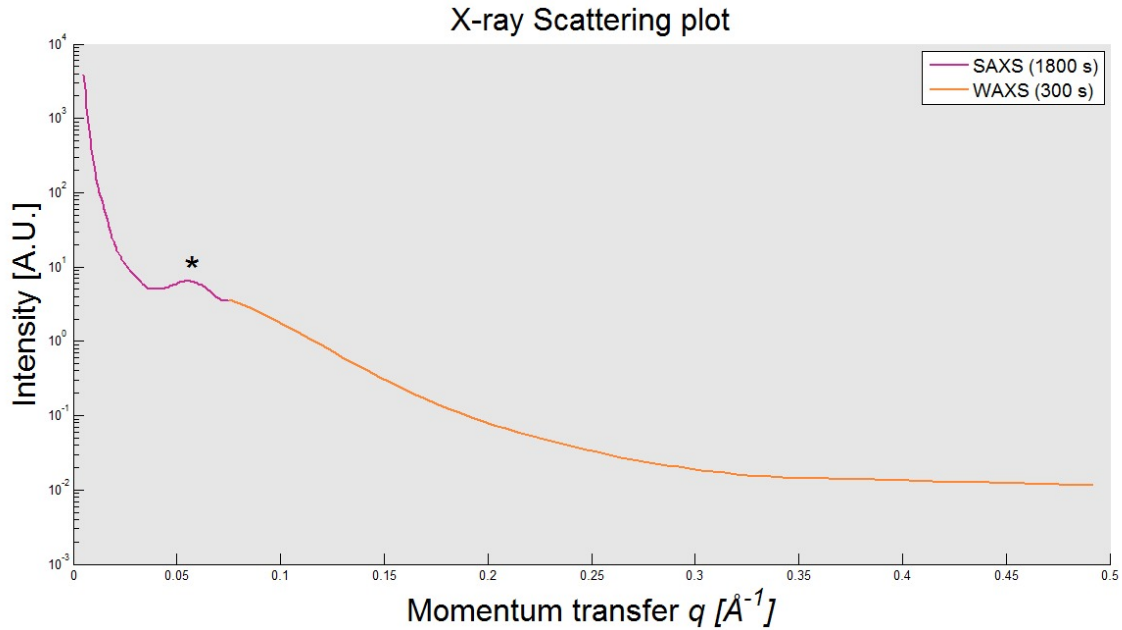


Figure 3.9: X-ray scattering plot highlighting both the SAXS (purple curve) and WAXS (light-orange curve) contribution in the range $q = 0.005 - 0.5 \text{ \AA}^{-1}$. The * symbol highlights the characteristic bump, occurring at a q -value $q = 0.05433 \text{ \AA}^{-1}$.

For the sake of completeness, Fig. 3.10 reports the scattering pattern detected during SAXS, which yields the afore-discussed purple curve in Fig. 3.9 when integrated along the radial direction.

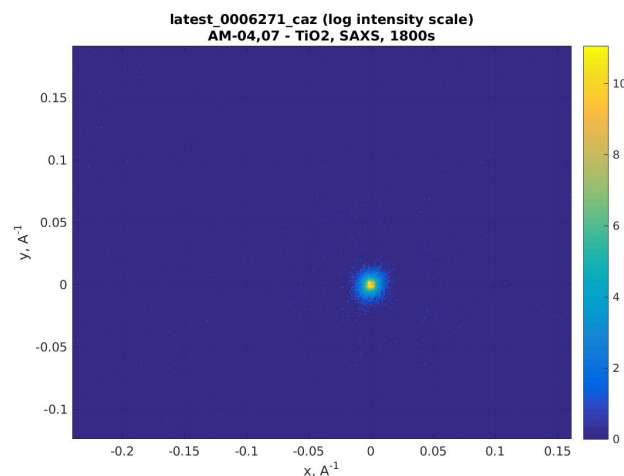


Figure 3.10: Scattering pattern revealed on the detection window during SAXS run.

3.1.6 Drug uptake and release

3.1.6.1 Loading and elution test in cuvette

During the loading, the samples were monitored closely and all the data have been collected in Table 3.2.

Readings	1 st : 18 h	2 nd : 24 h	3 rd : 41.5 h	4 th : 42 h
Stock Solution	1.51–1.45–1.42* (1045–1003–982.7)	—	—	—
Cuvette A	1.34–1.30–1.30 (927.3–899.7–899.7)	1.39–1.35–1.41 (961.9–934.3–975.8)	1.53–1.47–1.46 (1059–1017–1010)	1.54–1.57–1.56 (1066–1087–1080)
Cuvette B	1.39–1.33–1.35 (961.9–920.4–934.3)	1.56–1.54–1.53 (1080–1066–1059)	1.45–1.41–1.44 (1003–975.8–996.5)	1.61–1.57–1.57 (1114–1087–1087)

Table 3.2: Loading readings. The absorbance value (first line of each cell) corresponds to a 20-times diluted drop coming from the bulk of the cuvette. The corresponding actual concentration is presented in brackets expressed in μM .

* The stock value was measured at the beginning of the loading test as a "0 h" reference value.

As the main purpose of the loading experiment was to show the general trend, the time intervals between the measurements are rather broad. What we can conclude from this is that, after an initial "implosion" of the concentration with respect to the initial concentration (stock solution), both the cuvettes approached the latter gradually and not always smoothly. During the experiment we faced some mild but unavoidable PBS evaporation, which led to an increase of apparent concentration, thus being the most reasonable explanation for the values that exceeded the stock reference concentration. This evaporation is also confirmed by the final volume left in the cuvette after the experiment, being ~ 3.0 ml vs the initial 3.3 ml. After 42 h, we claimed that the solution had approached the stock value and had settled at that. Therefore, the values in blue in Table 3.2 have been used for further estimations. Interestingly enough, when translating the numbers into their physical meaning, it seems as though the Iopamidol immediately gets into the pores (therefore explaining the initial decrease of the bulk concentration we even faced in the runs we deemed as failed) and then gets gradually and partly replaced by PBS, until a state of thermodynamic equilibrium occurs. In other words, after an initial uneven loading, it might be even possible that some elution got triggered during the test.

The elution test is definitely much more interesting and special attention was dedicated in the initial phase of the experiments. The general trend coming from data elaboration is reported in Fig. 3.11. The two curves have the role of highlighting short-term (run 2) and long-term (run 1) evolution of the drug release. After 8 hours no significant absorbance changes were measured in run 2. If considering that the final concentration for run 1 was $12.03 \mu\text{M}$ after 50.25 hours (compared to $13.7 \mu\text{M}$ in 8 hours for run 2), we can claim that less than 10 hours are sufficient for the elution test with decent approximation. The final volume after removing the support+slides setup was 2.8 ml for both runs. Therefore, as a rough estimation, the total eluted moles is equal to $13.67 \mu\text{M} \cdot 2.8 \text{ ml} = 38.3 \text{ nmoles}$

(run 1) and $12.03 \mu\text{M} \cdot 2.8 \text{ ml} = 33.7 \text{ nmoles}$ (run 2). Considering that we used six slides coated on both sides, the total eluted moles per surface is $\sim 3.19 \text{ nmoles}$ and $\sim 2.81 \text{ nmoles}$, which looks rather consistent.

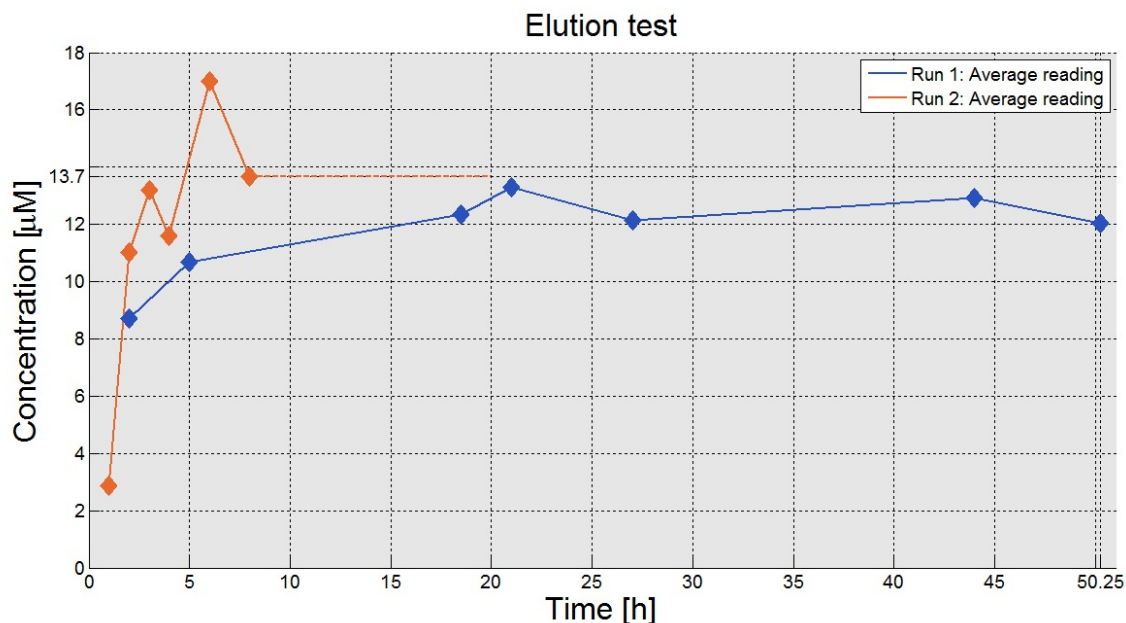


Figure 3.11: Resulting plots from two distinct runs of the elution test. Both curves show the average reading coming from the respectively examined cuvettes. No significant changes in the trend were detected after 8 hours from the beginning of the test for the orange curve, hinting that the concentration of the bulk settled to the value of $13.7 \mu\text{M}$. The second run focuses on long-term evolution and eventually settles at $12.03 \mu\text{M}$ after 50.25 hours.

3.1.6.2 QCM-D

All the data acquired from QCM-D are reported in picture Fig. 3.12.

A huge difference in trend between control samples and coated sensors immediately stands out. During the whole test the non-coated titanium sensors showed little to no adsorption/release of the drug, as both mass and dissipation kept fluctuating around the same value. This is expected, since none of the sensors had a mesoporous texture to carry the load. On the other hand, both of the coated samples exhibited a significant and consistent change in mass. More interestingly, a mass drop clearly emerged after elution with PBS had started (right of vertical dashed line). The machine registered about $-\Delta 8 \text{ ng cm}^{-2}$ for Coated-1 and around $-\Delta 3 \text{ ng cm}^{-2}$ with strong oscillations for Coated-2. However, we were aware of some machine-related inherent drifts in signal detection, therefore we claim that this information may be a large underestimation of the actual mass eluted away. As a matter of fact, one can observe that the mass kept increasing linearly even during elution, which is not intended. A possible reason may be the presence of residual uncalcinated organic phases, which could gradually swell as the layer is exposed to the solution. Nevertheless, taking into account what reported in Section 3.1.6.1, the eluted

3. Results

moles were ~ 3 nmoles, which translates into $8.6 \times 10^3 \text{ ng cm}^{-2}$ by means of simple algebraic manipulations. A major difference between these two measurements is the static load vs dynamic load the sensors experienced in cuvette vs QCM-D respectively. However, the three orders of magnitudes difference leaves the matter open for speculations. No significant jumps in dissipation were observed during the whole test, meaning that the viscosity of the mesoporous layer was not visibly altered by the inflow/outflow of the two prepared solutions.

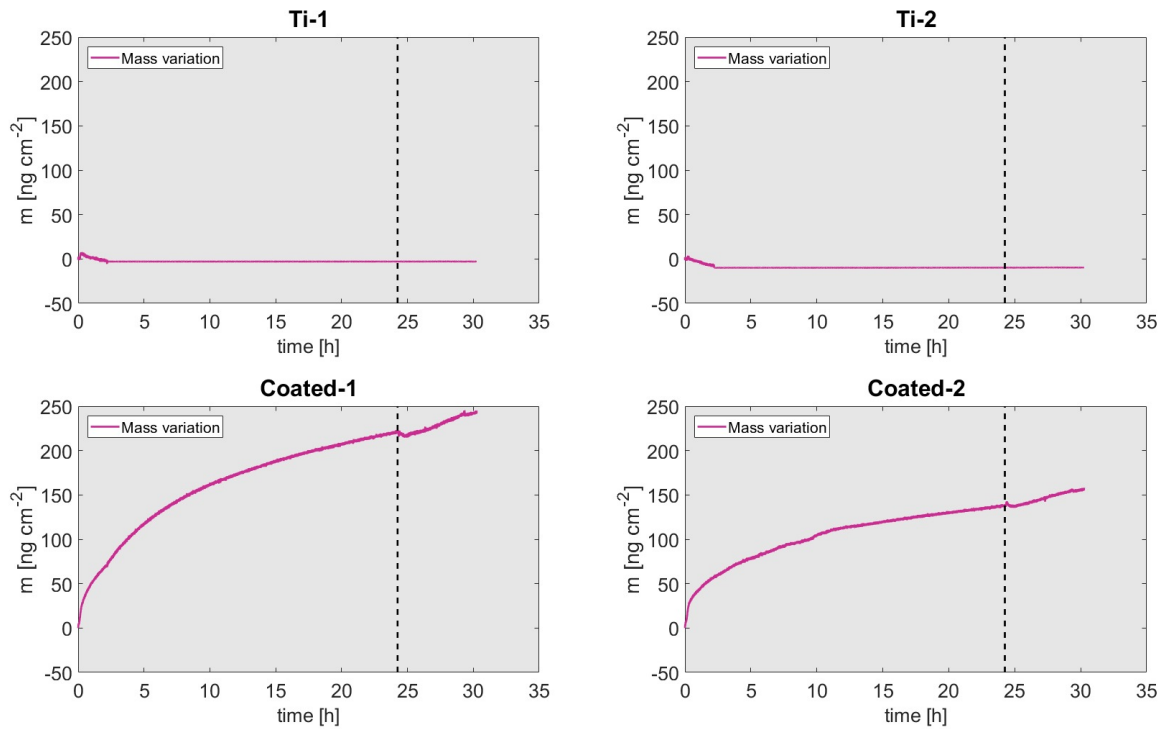


Figure 3.12: Plots of mass corresponding to the four sensors used for QCM-D. The shift in frequency has been converted to shift in mass according to equation 2.4. A vertical black dashed line is shown to separate the loading region (left) from the elution region (right). Ti-1 and Ti-2 refer to the control non-coated samples.

3.2 Drug testing with MRI - first approach

The novelty of the selected technique for this work set several challenges to overcome. The choice of field intensity, temperature, the presence of background noise ascribable to the samples (e.g. titania, Poloxamer, residual phases) and/or contaminants are all factors to be dealt with. Since there is not a consolidated mastery, to our knowledge, available worldwide for CEST, it was not possible to examine successfully all the samples produced in the intended time frame. However, it is worth presenting what we managed to gather so far, as a possible first step for future improvement.

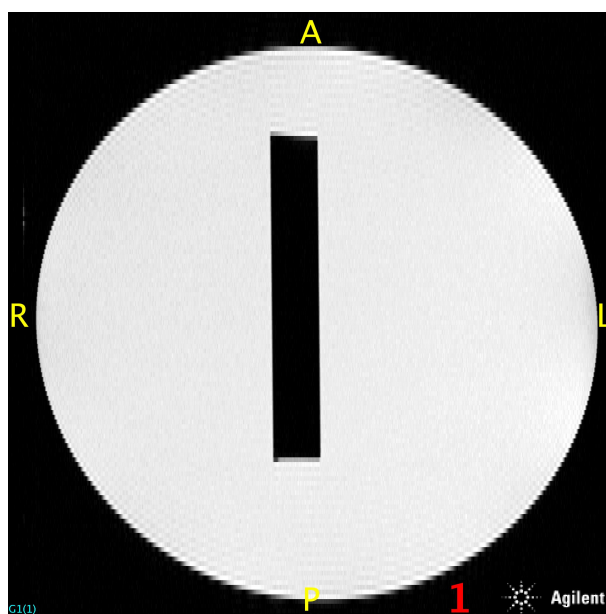


Figure 3.13: Cross-section of an examined glass slide (loaded and dipped in the gel at $\text{pH} = 7.4$).

Fig. 3.13 shows our first attempt for validating our strategy on a loaded sample (dipped in the $\text{pH} = 7.4$ gel at $18\text{ }^{\circ}\text{C}$). At first glance, the examined slide appears totally dark and does not show the expected differences in hue. This could stem from many reasons. Possibly, the most important ones are the following:

- The amount of Iopamidol hosted in the pores is insufficient to provide a sufficiently intense signal, despite the high magnetic field used.
- The drug needs more time to interact with the surrounding gel
- A suppression of interference by Poloxamer and the other materials present on the sample must be performed during image processing.
- The temperature affects protons mobility, hence the exchange rate.

Therefore, an extensive experimental work is required and some key features, such as loading time and Iopamidol concentration, must be correctly adjusted. Unfortunately, it was not possible to present the other pH levels for comparison.

4. Discussion

The extensive characterisation study performed on the mesoporous layer we produced brought important considerations but, at the same time, gave rise to challenges and open questions. From SEM and TEM (Section 3.1.1) it is clear that the adopted protocol led successfully to a mesoporous and randomly-ordered structure. It was evident from microscopy that the coating is sufficiently thin and that the pore size distribution appears to be rather narrow and unimodal. Such claim was further confirmed by BET analysis (Section 3.1.2) and SAXS (Section 3.1.5), which both reported a pore size around 6 nm. However, BET was strongly affected by the presence of glassy contaminants that influenced negatively the readings for specific surface area and free volume available. Glass shards are indeed flat, massive and non-porous, thus increasing total mass with respect to the free surface available. For this reason, it is safe to assume the quantitative results derived from BET as lower bounds for the respective properties. As final comment for the structure, no symmetry was detected with SAXS, which confirms the hypothesis of long-range order.

A crucial requirement for the titania coating is having a good interaction with the selected drug. From XPS (Section 3.1.4), the chemical composition is significantly different between loaded and non-loaded samples in terms of secondary species. We showed that the latter contained extra ionic compounds deriving from the salts dissolved in PBS used for loading. On top of that, the carbon content, albeit smaller, was the result of a complex overlapping of different hybridisation states. This proves the complexity of the chemical environment in which carbon lies, which is a clear evidence of the presence of Iopamidol (aromatic rings). The surprisingly high amount of carbon detected in the non-loaded sample could only be ascribable to uncalcinated residual micelles or to the formation of contaminants during preservation. The difference in nitrogen contribution is minor and possibly also due to organic traces. A possible contribution from the nitrogen atoms in the drug is to be expected as well. Despite these differences, the prevalent structure for both of the samples corresponds to titania. This is confirmed by XRD (Section 3.1.3), which spectrum allowed concluding that anatase is the main crystalline phase in our sample, with marginal contributions of rutile and, possibly, brookite. Although, it must be noted that the crystallinity is rather limited, and that is visually clear from TEM images.

A good interaction with the drug is observed in loading/elution tests performed both in cuvette and with QCM-D (refer to Section 3.1.6.1 and Section 3.1.6.2 respectively). In both cases we confirmed that the coating is functional and amenable to loading. However, the conflicting data gathered from several attempts in cuvette and QCM-D did not allow us to draw solid quantitative conclusions with respect to kinetics and elution. It would appear that the coating is ready to give off drug in the very first hours of elution, whereas it settles and retains most of the drug. The cuvette test was inherently influenced by evaporation and irregularities in the bulk of the solution, which led to hardly addressable inconsistencies. Another source of misinterpretation could have been the equilibrium between loading and elution. That is to say that we are unsure whether the bulk Iopamidol

concentration is reflected in the pores or the drug gets replaced by PBS over time and vice versa. It would be relevant to perform more analyses on that in the future, in order to properly adjust the loading step and, consequently, the quality of MRI mapping. The major problem with QCM-D was the constant drift in the readings, that dampened the elution burst down. This linear drift has been encountered in other measurements involving mesoporous structures performed in our lab, however its origin is still unclear. A plausible explanation might be the presence of residual organic compounds, which may swell over time and, hence, retain PBS even during elution. More efforts could be made in the future of this project to achieve full comprehension of all these phenomena.

MRI is for sure the most interesting part of this work: the single picture presented above in this thesis represents just the beginning of the validation of our idea. The apparent total darkness of the tested sample suggests several adjustments. It is possible that the Iopamidol present in the pores was insufficient. Such obstacle may be addressed by changing the preparation protocol for the slides, perhaps by loading them with increased drug concentration and over an extended period of time. The MRI experiment could be performed under different conditions (longer time to allow the drug to interact with the gel, higher temperature). Since, to our knowledge, this is the first time that mesoporous titania coatings are exploited in conjunction with MRI-CEST, we are not aware yet of the implications on the detected signal and consequent manipulation thereof. Possibly, the ratiometric approach would require a correction factor and/or the noise coming from the other materials present in the setup must be appropriately suppressed. In spite of all of these difficulties, we are rather satisfied with the way the setup for MRI was designed and produced.

5. Conclusion

5.1 General considerations

In this work we successfully explored the key-properties of a mesoporous titania layer produced by dip-coating, which seemed to possess rather solid characteristics. Although the time constraint slightly affected the accuracy and depth of our analysis, the presented results agree with our expectations and other studies available in the literature, thus providing a convincing evidence that we produced a suitable material for the intended task. Although Iopamidol is a promising contrast agent for this application, both the difficulties encountered in the realisation of the experiments and the novelty of CEST, set up open challenges for validating the concept and leave large room for further studies and speculations.

5.2 Future perspectives and ideas

Together with presenting a first impression of what to expect from the strategy adopted, this work takes the role of a starting point for an extensive experimental follow-up. It could be interesting to repeat the setup used for MRI with in situ grown bacteria for a more realistic acidic environment. Further investigation of drug responsiveness loaded into titanium screws in ex vivo bones may be a precious extension of this study too. The interaction of Iopamidol with a living organism must be necessarily tested in vivo, with respect to diffusion in surrounding tissues and signal readability. It is even plausible that a different immobilisation technique must be harnessed to hold Iopamidol in place for longer time, thus allowing the physician to assess the status of the implant on-demand and repeatedly.

In conclusion, we claim that this approach has tremendous potential to contribute substantially in detection of infections and we are also convinced that the goal of setting a first starting point in this direction has been fulfilled.

Bibliography

- [1] Bozic, Kevin J., et al. "The epidemiology of revision total hip arthroplasty in the United States." *JBJS* 91.1 (2009): 128-133.
- [2] Zhuang, Hongming, et al. "The promising role of 18F-FDG PET in detecting infected lower limb prosthesis implants." *Journal of Nuclear Medicine* 42.1 (2001): 44-48.
- [3] Pill, Stephen G., et al. "Comparison of Fluorodeoxyglucose Positron Emission Tomography and 111Indium-White Blood Cell Imaging in the Diagnosis of Periprosthetic Infection of the Hip." *The Journal of arthroplasty* 21.6 (2006): 91-97.
- [4] Williamson, M. R., et al. "111 In-labeled leukocytes in the detection of prosthetic vascular graft infections." *American Journal of Roentgenology* 147.1 (1986): 173-176.
- [5] Gemmel, Filip, et al. "Prosthetic joint infections: radionuclide state-of-the-art imaging." *European journal of nuclear medicine and molecular imaging* 39.5 (2012): 892-909.
- [6] Online source: <https://www.insideradiology.com.au/pet-scan/> retrieved on May 15th 2019.
- [7] Longo, Dario Livio, et al. "Iopamidol as a responsive MRI-chemical exchange saturation transfer contrast agent for pH mapping of kidneys: in vivo studies in mice at 7 T." *Magnetic resonance in medicine* 65.1 (2011): 202-211.
- [8] Longo, Dario L., et al. "A general MRI-CEST ratiometric approach for pH imaging: demonstration of in vivo pH mapping with iobitridol." *Journal of the American Chemical Society* 136.41 (2014): 14333-14336.
- [9] Longo, Dario Livio, et al. "Imaging the pH evolution of an acute kidney injury model by means of iopamidol, a MRI-CEST pH-responsive contrast agent." *Magnetic resonance in medicine* 70.3 (2013): 859-864.
- [10] Hoerr, Verena, and Cornelius Faber. "Magnetic resonance imaging characterization of microbial infections." *Journal of pharmaceutical and biomedical analysis* 93 (2014): 136-146.
- [11] Zhou J, Payen JF, Wilson DA, Traystman RJ, van Zijl PC. Using the amide proton signals of intracellular proteins and peptides to detect pH effects in MRI. *Nat Med* 2003;9:1085–1090.
- [12] Arciola, Carla Renata, et al. "Implant infection and infection resistant materials: a mini review." *The International journal of artificial organs* 28.11 (2005): 1119-1125.
- [13] Maderazo, EUFRONIO G., S. U. S. A. N. Judson, and H. E. R. B. E. R. T. Pasternak. "Late infections of total joint prostheses. A review and recommendations for prevention." *Clinical orthopaedics and related research* 229 (1988): 131-142.
- [14] Xia, Wei, et al. "Mesoporous titanium dioxide coating for metallic implants." *Journal*

- of Biomedical Materials Research Part B: Applied Biomaterials 100.1 (2012): 82-93.
- [15] Karlsson, Johan, et al. "In vivo biomechanical stability of osseointegrating mesoporous TiO₂ implants." *Acta biomaterialia* 8.12 (2012): 4438-4446.
- [16] Brinker, C. Jeffrey, et al. "Evaporation-induced self-assembly: nanostructures made easy." *Advanced materials* 11.7 (1999): 579-585.
- [17] Atefyekta, Saba, et al. "Antimicrobial performance of mesoporous titania thin films: role of pore size, hydrophobicity, and antibiotic release." *International journal of nanomedicine* 11 (2016): 977.
- [18] Karlsson, Johan, Saba Atefyekta, and Martin Andersson. "Controlling drug delivery kinetics from mesoporous titania thin films by pore size and surface energy." *International journal of nanomedicine* 10 (2015): 4425.
- [19] Karlsson, Johan, et al. "Ex vivo alendronate localization at the mesoporous titania implant/bone interface." *Journal of Materials Science: Materials in Medicine* 26.1 (2015): 11.
- [20] Ebadi, Amanollah, Jafar S. Soltan Mohammadzadeh, and Anvar Khudiev. "What is the correct form of BET isotherm for modeling liquid phase adsorption?." *Adsorption* 15.1 (2009): 65-73.
- [21] Online source:
https://serc.carleton.edu/research_education/geochemsheets/techniques/XRD.html
retrieved on April 24th 2019
- [22] Huang, Xianhe, et al. "A practical model of quartz crystal microbalance in actual applications." *Sensors* 17.8 (2017): 1785.
- [23] AlOthman, Zeid. "A review: fundamental aspects of silicate mesoporous materials." *Materials* 5.12 (2012): 2874-2902.
- [24] Broekhoff, J. C. P. "Mesopore determination from nitrogen sorption isotherms: Fundamentals, scope, limitations." *Studies in Surface Science and Catalysis*. Vol. 3. Elsevier, 1979. 663-684.
- [25] Galkina, O. L., et al. "Surfactant-assisted sol-gel synthesis of TiO₂ with uniform particle size distribution." *International Journal of Inorganic Chemistry* 2011 (2011).
- [26] Cai, Jianchao, and Xiangyun Hu, eds. *Petrophysical Characterization and Fluids Transport in Unconventional Reservoirs*. Chapter 1, Elsevier, 2019.
- [27] Karlsson, Johan, Saba Atefyekta, and Martin Andersson. "Controlling drug delivery kinetics from mesoporous titania thin films by pore size and surface energy." *International journal of nanomedicine* 10 (2015): 4425.
- [28] Joshi, Meenal M., et al. "Visible light induced photoreduction of methyl orange by N-doped mesoporous titania." *Applied Catalysis A: General* 357.1 (2009): 26-33.
- [29] Fei, Hailong, et al. "Selective synthesis of borated meso-macroporous and mesoporous spherical TiO₂ with high photocatalytic activity." *Microporous and Mesoporous Materials* 102.1-3 (2007): 318-324.

- [30] Kumler, W. D., and John J. Eiler. "The acid strength of mono and diesters of phosphoric acid. The n-alkyl esters from methyl to butyl, the esters of biological importance, and the natural guanidine phosphoric acids." *Journal of the American Chemical Society* 65.12 (1943): 2355-2361.

A. Appendix A: Gel preparation for MRI

Every buffer solution was prepared with a volume of 30 ml and 0.1 M strength. For calculations, Henderson-Hasselbalch equation (A.1) was used:

$$pH = pK_{a_2} + \log \left(\frac{[HPO_4^{2-}]}{[H_2PO_4^-]} \right) \quad (A.1)$$

where pK_{a_2} was chosen as 6.82 [30] and the concentrations in \log 's argument are coming from Sodium phosphate dibasic heptahydrate ($Na_2HPO_4 \cdot 7H_2O$, numerator) and Sodium phosphate monobasic dihydrate ($NaH_2PO_4 \cdot 2H_2O$, denominator). Table A.1 conveniently summarises all the steps used for the preparation of the buffers.

pH 7.4	pH 7.0
<ol style="list-style-type: none"> 1. Put 24 mL of Milli-Q water in a beaker 2. Add 0.606 g of $Na_2HPO_4 \cdot 7H_2O$ 3. Add 0.115 g of $NaH_2PO_4 \cdot 2H_2O$ 4. Adjust with Milli-Q until 30 mL 5. Adjust pH if necessary 	<ol style="list-style-type: none"> 1. Put 24 mL of Milli-Q water in a beaker 2. Add 0.465 g of $Na_2HPO_4 \cdot 7H_2O$ 3. Add 0.198 g of $NaH_2PO_4 \cdot 2H_2O$ 4. Adjust with Milli-Q until 30 mL 5. Adjust pH if necessary
pH 6.5	pH 6.0
<ol style="list-style-type: none"> 1. Put 24 mL of Milli-Q water in a beaker 2. Add 0.287 g of $Na_2HPO_4 \cdot 7H_2O$ 3. Add 0.301 g of $NaH_2PO_4 \cdot 2H_2O$ 4. Adjust with Milli-Q until 30 mL 5. Adjust pH if necessary 	<ol style="list-style-type: none"> 1. Put 24 mL of Milli-Q water in a beaker 2. Add 0.110 g of $Na_2HPO_4 \cdot 7H_2O$ 3. Add 0.404 g of $NaH_2PO_4 \cdot 2H_2O$ 4. Adjust with Milli-Q until 30 mL 5. Adjust pH if necessary
pH 5.5	
<ol style="list-style-type: none"> 1. Put 24 mL of Milli-Q water in a beaker 2. Add 0.039 g of $Na_2HPO_4 \cdot 7H_2O$ 3. Add 0.445 g of $NaH_2PO_4 \cdot 2H_2O$ 4. Adjust with Milli-Q until 30 mL 5. Adjust pH if necessary 	

Table A.1: Preparation steps followed for the buffers used for the MRI test.

All the gels were produced by adding 30% wt. of Lutrol[®] F127 Poloxamer 407 to 2.330 ml PBS and by stirring vigorously with the aid of a centrifuge (3000 rpm, 30 minutes, -9°C) to achieve a homogeneous and bubble-free substance. The temperature was chosen so as to decrease the viscosity of the gel and, consequently, to ease the release of inherent gas bubbles trapped in the network. When necessary, 54.3 mg of Iopamidol were added to the buffers (*i.e.* for the three control vials).